Nanoscale

REVIEW

Cite this: *Nanoscale*, 2025, **17**, 7552

Recent progress on transition metal dichalcogenide-based composites for cancer therapy

Bo Chen, * Yue Dai, Suxiang Yang, Chunhong Chen* and Lianhui Wang *

Received 31st December 2024,
Accepted 25th February 2025

DOI: 10.1039/d4nr05510a

rsc.li/nanoscale

Cancer remains a global health challenge, driving the need for advanced treatments. While transition metal dichalcogenides (TMDs) show promise in cancer therapy, their stability and efficacy require improvement. This study explores TMD-based composites as a solution to enhance their therapeutic potential. This review begins by providing an overview of TMDs and emphasizing their preparation techniques and fundamental properties. The focus is then shifted to categorizing TMD-based composites based on their constituent materials, delving into various types, such as TMD-organic, TMD-carbon, TMD-metal chalcogenide, TMD-metal, and TMD-oxide composites, as well as more complex ternary and multinary systems. We further explore key fabrication strategies, including hydrothermal/solvothermal methods and surface deposition/coating techniques. Subsequently, the focus shifted to their applications in cancer treatment, including chemotherapy, photothermal therapy, phototherapy, and integrated combination therapies. Finally, critical challenges in the field and perspectives on potential directions for future research are presented.

1. Introduction

Cancer therapy remains a pivotal focus in biomedicine.[1,2] As the global incidence of cancer continues to rise, the imperative for the development of pertinent diagnostic[3,4] and therapeutic methods[5–7] is escalating.[8] In the course of treatment, researchers should not only assess the therapeutic effectiveness, but also prioritize the safety and feasibility of interventions.

State Key Laboratory of Flexible Electronics & Jiangsu Key Laboratory of Smart Biomaterials and Theranostic Technology, Institute of Advanced Materials (IAM), School of Chemistry and Life Sciences, Nanjing University of Posts and Telecommunications, Nanjing 210023, China. E-mail: iambchen@njupt.edu.cn, iamcch@njupt.edu.cn, iamlhwang@njupt.edu.cn

Bo Chen

Bo Chen received his B.S. degree, M.S. degree, and Ph.D. degree from Lanzhou University (2009), Shandong University (2012), and Nanyang Technological University (2017), respectively. Then, he worked as a research fellow at Nanyang Technological University (2017–2020) before moving to the City University of Hong Kong as a research associate (2020–2023). Currently, he is a Professor at the School of Chemistry and Life Sciences, Nanjing University of Posts and Telecommunications. His current research interests include the synthesis, characterization, and applications of nanomaterials with unconventional phases.

Yue Dai

Yue Dai received a B.S. degree from Tongda College, Nanjing University of Posts and Telecommunications in 2022. She is currently pursuing her M. S. degree at the School of Materials Science and Engineering, Institute of Advanced Materials, Nanjing University of Posts and Telecommunications, under the supervision of Prof. Bo Chen. Her research interests include the preparation of TMD-based materials and their biomedical applications.

Hence, there is a pressing need to rationally design materials tailored for cancer therapeutics.

Over the last two decades, two-dimensional (2D) transition metal dichalcogenides (TMDs) have been drawing close attention from researchers[9–11] due to their unique electronic and optical properties,[12–14] establishing them as promising candidates for biomedicine.[15–17] Compared with some other 2D nanomaterials that have been utilized in cancer therapies, *e.g.*, graphene,[18–20] layered double hydroxides (LDHs),[21–23] and black phosphorus (BP),[24–27] the tunable bandgap along with outstanding physicochemical properties endows TMDs with a wider scope of anti-tumor applications.[28–30] Their affordability and exceptional biocompatibility further contribute to their appeal.[31,32] For instance, MoS_2 nanomaterials have been extensively investigated as outstanding photothermal agents along with X-ray computed tomography (CT) imaging agents.[33] It is worthy of note that TMDs exhibit low toxicity when serve as therapeutic platforms, thanks to their rapid biodegradation and safe excretion.[34] Additionally, TMDs display superior near-infrared (NIR) light absorption, enhanced optical stability, and greater photothermal conversion efficiency compared to gold nanoparticles. These attributes make them more suitable for imaging-guided photothermal therapy (PTT).[35]

Despite TMDs have plenty of prominent physicochemical properties, their limited serum stability and inefficient intracellular delivery efficiency may pose constraints on their biomedical applications.[36] To address these challenges, researchers have adopted various strategies of surface modifications for TMDs.[8,37,38] Through the decoration with biocompatible and nontoxic materials, TMDs have been shown to exhibit enhanced stability in phosphate-buffered saline (PBS).[39] Over and above, it has been demonstrated that it is an effective approach to combine TMDs with various other functional materials, forming unique hybrids that exhibit higher efficiency in anti-tumor treatment.[36,40,41]

In this review, we present a succinct introduction of TMDs and their synthesis. The subsequent discussion focuses on categorizing the TMD-based composites based on their components. Detailed insights are provided for various composite types, including TMD-organic material composites, TMD-carbon composites, TMD-metal chalcogenide composites, TMD-metal composites, TMD-oxide composites, and TMD-based ternary and multinary compounds. Following this, we delve into the preparation methods of TMD-based composites, which typically involve hydrothermal/solvothermal methods or surface deposition/coating. Subsequently, the focus shifts to their applications in cancer therapy, including chemotherapy, PTT, phototherapy, and combination therapy. Finally, we present the challenges faced in this research direction and discuss the prospects for these endeavors.

2. Transition metal dichalcogenides

The chemical formula of TMDs is MX_2,[42] indicating a hexagonal bonding structure with a sandwich-type X–M–X arrangement.[13,43,44] In this formula, X refers to the sulfur group elements while M denotes to the transition metal elements (Fig. 1A and B).[45] Due to the weak van der Waals forces governing the bonding between TMD layers, their monolayered flakes can be exfoliated *via* a strategy akin to that employed for graphene.[13]

It should be noted that because of the diverse spherical coordination of transition metals elements, TMDs display a variety of phase structures.[9,44,46–48] The most common phase structures include the hexagonal 2H phase, as well as the octahedral 1T and rhombohedral 3R phases (Fig. 1C).[44] Besides, there is a variant known as the distorted phase 1T′ characterized by a distorted octahedral structure (Fig. 1D).[49]

The preparation methods of 2D TMDs can be broadly classified into top-down and bottom-up strategies.[50–53] Top-down strategies can be further categorized based on force sources, including mechanical exfoliation, ultrasonic exfoliation, and

Chunhong Chen

Chunhong Chen received her Ph.D. from Zhejiang University in 2019, working on porous carbonaceous materials for application in catalysis and energy storge. She then joined the Institute for Basic Science, Korea, and the Hong Kong Polytechnic University as a postdoctoral fellow (2019–2023). She is currently a Professor at the Nanjing University of Posts and Telecommunications, and her research interests are mainly focused on the controllable preparation of functional carbonaceous materials and polyoxometalate-based micro-/nano-architecture.

Lianhui Wang

Lianhui Wang is a Professor at the State Key Laboratory of Flexible Electronics, Nanjing University of Posts and Telecommunications. He is a distinguished professor of Cheung Kong Scholars. He presided over more than 30 domestic and international scientific research projects, such as the National Outstanding Youth Fund, key projects of the National Natural Science Fund, the national major scientific research project, etc. He has long been engaged in teaching and research in the fields of photoelectric nanomaterials, bioptoelectronics, and nanobiological medicine.

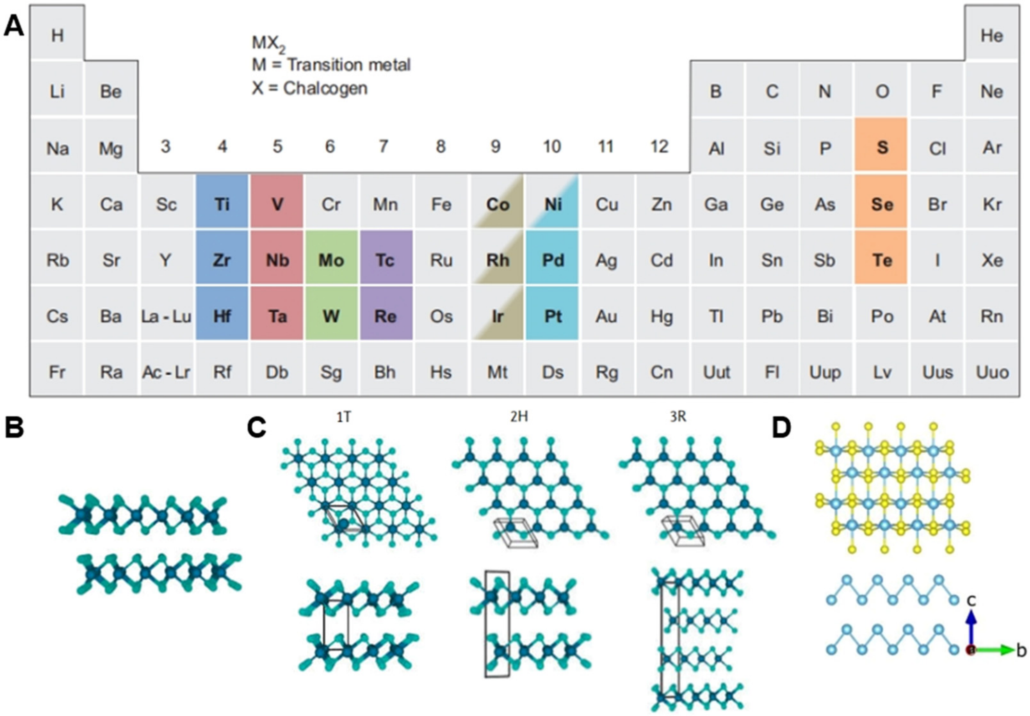

Fig. 1 Composition and structure of TMDs. (A) The elemental composition of TMDs.[43] Reproduced with permission from ref. 43. Copyright 2013 Springer Nature. (B) Sandwich TMD structure (C) Phase structures of TMDs. Top view (top) and side view (bottom) depicting the octahedral (1T), hexagonal (2H), and rhombohedral (3R) phases. The black lines delineate the unit cells of these lamellar structures.[44] Reproduced with permission from ref. 44. Copyright 2020 Springer Nature. (D) Top and side views of the distorted 1T′ WS_2 phase. The upper panel illustrates the in-plane crystal structure of monolayer 1T′-WS_2, whereas the lower panel displays the zigzag chain of W atoms.[49] Reproduced with permission from ref. 49. Copyright 2023 American Association for the Advancement of Science (AAAS).

electrochemical exfoliation. On the other hand, bottom-up strategies encompass chemical vapor deposition (CVD),[54] physical vapor deposition (PVD), and hydrothermal/solvothermal methods.[55]

Fig. 2A shows a diagram of the preparation of few-layer $MoTe_2$ crystals through the CVD method.[42] The metal precursor compounds, MoO_3 and NaCl, were placed in the center of a quartz tube and the Si/SiO_2 substrate was placed on an alumina boat with the polished side facing down. Another alumina boat containing tellurium (Te) powder was placed on one side of the quartz tube, and a mixture of H_2 and Ar was used as the carrier gas. After the reaction, the mixture was allowed to cool to room temperature. The obtained $1T_d$ phase $MoTe_2$ had an in-plane crystal structure and displayed vertical stacking.

PVD is another typical method used for preparing 2D TMDs. Under high vacuum conditions and appropriate temperatures, bulk TMDs (*e.g.*, MoS_2 powder) can be evaporated into gaseous molecules, which are deposited onto the surface of the substrate with temperature drops.[56,57] As one of the most representative PVD methods, molecular beam epitaxy (MBE) (Fig. 2B) has received widespread attention. Generally, during epitaxial growth, the lattice structure of the substrate affects the orientation of the film. Therefore, if the substrate and synthesized end materials meet eutectic conditions or lattice matching, high-quality films can be obtained. Whereas, TMDs do not require the lattice matching condition in principle when epitaxial growing since they do not process dangling bonds.[58]

Hydrothermal/solvothermal synthesis, as two similar synthesis methods,[59–61] can be used not only for the preparation of TMD dispersions, but also for the functionalization of TMDs simultaneously. These two methods are mainly conducted in sealed reactors lined with polytetrafluoroethylene, where precursors containing transition metals and sulfur group elements are mixed with water or organic solvents (Fig. 2C). As the temperature increases, high vapor pressure will be formed to promote the reaction.[62,63]

In contrast to bottom-up strategies, the typical top-down strategy for 2D TMDs is usually regarded as exfoliating bulk TMDs with a layered structure (Fig. 2D).[55] An Au-assisted exfoliation of 2D MoS_2 can be seen in Fig. 2E.[64] A thin layer of Au was deposited on the substrate, which was first covered with a thin Ti or Cr adhesion layer. Because of the good contact between the Au and layered bulk MoS_2 crystal on the tape, one or several large-area monolayer MoS_2 flakes remained on the Au surface when the adhesive tape was peeled off. However, the size of the available bulk crystals is limited, and thus the obtained monolayer flakes usually have macroscopic dimensions.

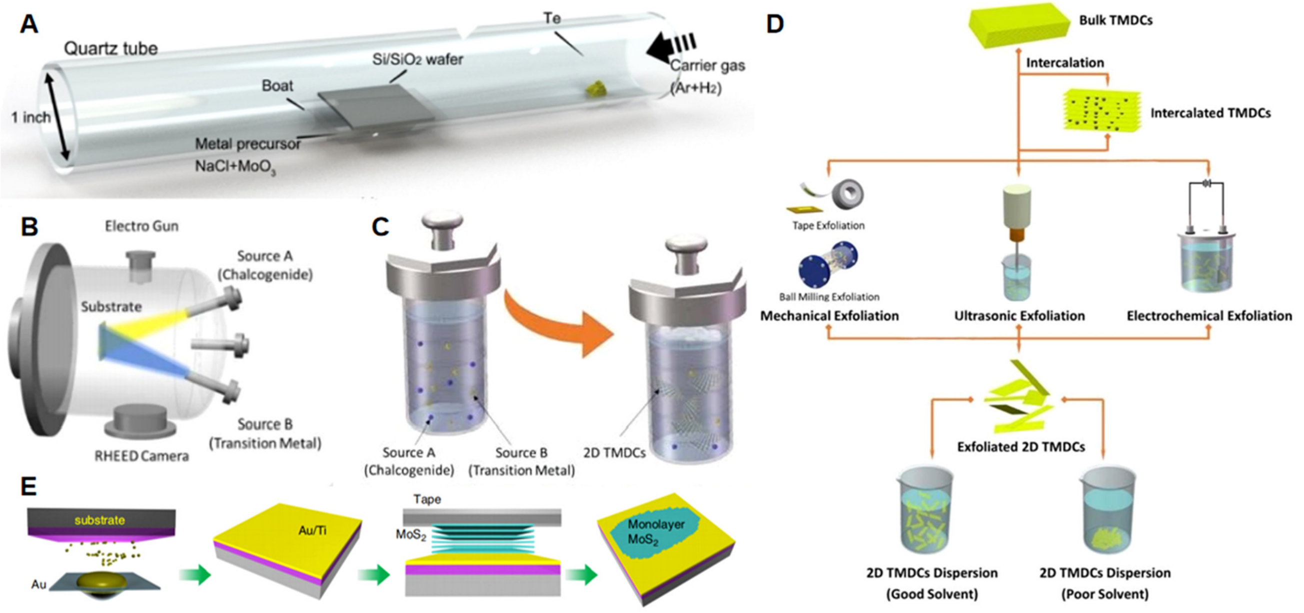

Fig. 2 Schemes of methods for the preparation of TMDs. (A) Schematic representation of the CVD method for preparing few-layer $MoTe_2$ crystals.[42] Reproduced with permission from ref. 42. Copyright 2019 Springer Nature. (B) Schematic illustration of the MBE method used to prepare TMDs. (C) Schematic illustration of the hydrothermal/solvothermal synthesis of TMDs. (D) Schemes of top-down strategies for TMDs.[55] Reproduced with permission from ref. 55. Copyright 2021 Elsevier. (E) Schematic illustration of Au-assisted exfoliation for synthesizing 2D MoS_2.[64] Reproduced with permission from ref. 64. Copyright 2020 Springer Nature.

3. Transition metal dichalcogenide-based composites

Because TMDs lack stability in the physiological environment[34,65] and have a relatively low intracellular delivery efficiency,[36] researchers have utilized various functional materials to modify TMDs to mitigate such difficulties. By integrating TMD materials with other functional materials, on one hand, the stability and biocompatibility of TMDs can be significantly enhanced, while on the other hand, this approach effectively addresses the limitations of low efficiency associated with single-component materials. In this section, we introduce TMD-based composites with constituent materials such as TMD-organic material composites, TMD-carbon composites, TMD-metal chalcogenide composites, TMD-metal composites, TMD-oxide composites, and TMD-based ternary and multinary compounds.

3.1. Transition metal dichalcogenide-organic material composites

As one of the most frequently employed materials for surface modification on TMDs, organic materials have the advantages of good biocompatibility and nontoxicity.[36] Organic materials commonly encompass polymers, for example, poly(ethylene glycol) (PEG)[66,67] and polyetherimide,[68,69] and small molecules, for example, chitosan (CS)[70,71] and L-cysteine.[72]

In a typical example, Liu *et al.* synthesized PEGylated MoS_2 nanosheets (Fig. 3A) for photothermal-chemo cancer therapy.[39] In their experiment, lipoic acid conjugated polyethylene glycol (LA-PEG) was used to functionalize 2D MoS_2 nanosheets after chemical exfoliation. With a disulfide group of LA-PEG anchored to surface defects of MoS_2, the physiological stability of MoS_2 in aqueous solutions was remarkably enhanced. MoS_2-PEG showed no obvious agglomeration in the PBS solution after centrifugation, while aggregation occurred with MoS_2 alone under the same treatment (Fig. 3B). Additionally, PEGylated MoS_2 exhibited a decrease in the lateral size and an increase in the average thickness compared to pristine MoS_2 (Fig. 3C). However, the UV-to-NIR absorbance was still strong upon PEG modification, which can be verified by UV-*vis*-NIR absorbance spectra. Moreover, this study examined the photothermal conversion efficiency of the as-obtained nanocomposites. As the photothermal heating curves shown, the temperature rose with the increasing laser power in the case of a low and constant concentration (0.03 mg mL^{-1}) of MoS_2-PEG solution.

To improve the biocompatibility and properties of MoS_2 nanosheets, Xu *et al.* utilized folic acid (FA) and lipoic acid (LA) functionalized hyperbranched polyglycerol (hPG) to conjugate on MoS_2 (FP-MoS_2, Fig. 3D and E).[65] With the existence of hPG and FA, the as-synthesized materials showed improved water dispersibility and higher cancer therapeutic efficiency. As shown in Fig. 3F, the stability of MoS_2 in PBS was significantly enhanced after FA/LA-hPG conjugation *via* disulfide bonds. The as-obtained FP-MoS_2 also displayed an excellent photothermal effect which could be adjusted by concentration and laser-power.[65]

Moreover, small molecules have also attracted the interest of many researchers due to their simple structure and small

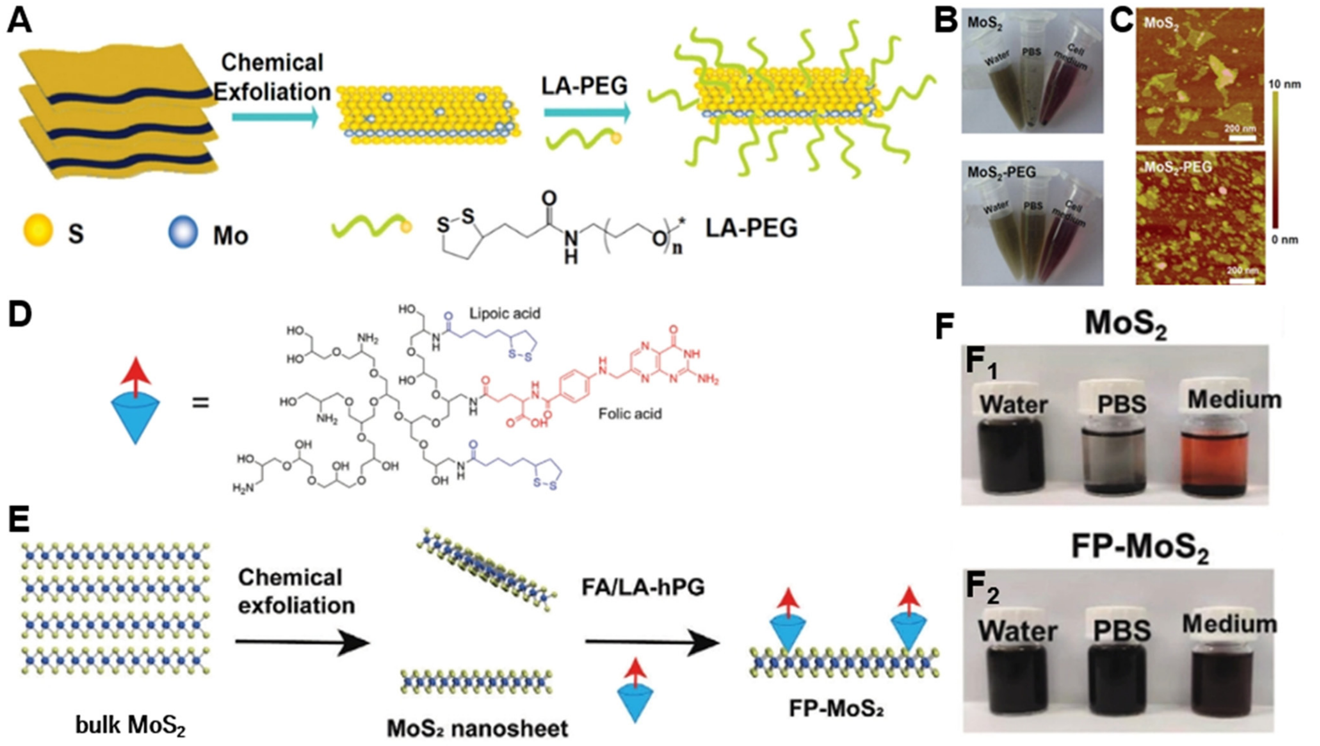

Fig. 3 Preparation and characterization of TMD-organic material composites. (A) Schematic diagram of the preparation of MoS_2-PEG nanosheets. (B) Photographs of MoS_2 (top) and MoS_2-PEG (bottom) after centrifugation at 3000 rpm in water, PBS, and cell medium. (C) Atomic force microscopy (AFM) images of MoS_2 (top) and MoS_2-PEG (bottom).[39] Reproduced with permission from ref. 39. Copyright 2014 Wiley-VCH. (D) Schematic illustration of the chemical structure of FA/LA-hPG. (E) Schematic illustration of the synthesis process of FP-MoS_2. (F) Photographs of MoS_2 (F_1) and FP-MoS_2 (F_2) dispersed in Milli-Q water, PBS, and Dulbecco's modified eagle's medium (DMEM) cell culture medium (containing 10% serum) for 7 days at 4 °C.[65] Reproduced with permission from ref. 65. Copyright 2021 Wiley-VCH.

site-blocking effect, which can make them easier and more controllable to biocouple on the surface of TMDs and improve the stability of TMDs during biochemical analysis.[73] Xie *et al.* chose egg yolk phospholipid, a representative of lipids, for modification on the surface of layered MoS_2 nanosheets so that it could offer a biocompatible protective barrier.[74] During the synthesis process, the lipid drew support from physical adsorption to coat on the as-prepared MoS_2 in order to obtain MoS_2-lipid nanocomposites following the rotary evaporation of liposomes. After a series of tests, it was found that the layered structure of MoS_2 did not change after modification (Fig. 4A). Clearly, MoS_2-lipid displayed better dispersibility in the three media than pristine MoS_2 (Fig. 4B). Meanwhile, the photothermal conversion efficiency of MoS_2 was not noticeably influenced by the lipid coating.

In another case, Shin *et al.* conjugated hyaluronate with MoS_2 (hyaluronate-MoS_2) for cancer therapy.[36] As a biocompatible natural material, hyaluronate was demonstrated to be equally capable of solving the low stability problem of MoS_2 nanosheets. In this nanocomposite, the disulfide bond acted as a link between MoS_2 and hyaluronate (Fig. 4C). As shown in the AFM images (Fig. 4D), the thickness and particle size of MoS_2 were all slightly increased owing to surface modification. Moreover, the obtained conjugates retained their crystal structure, as verified by transmission electron microscopy (TEM) images (Fig. 4E). In addition to the changes in morphology, dynamic light scattering analysis also revealed that hyaluronate-MoS_2 exhibited a dramatic improvement in stability. After 7 days in the presence of PBS, the sample with hyaluronate conjugation showed less aggregation and a smaller increase in size.

Beyond that, Zheng *et al.* proposed the use of gallic acid (GA) to modify MoS_2 nanosheets.[75] Upon preparing MoS_2 nanosheets *via* ultrasonic exfoliation, MoS_2@GA could be synthesized through strong π–π stacking. The prepared MoS_2@GA retained its nanosheet structure, with an average size of approximately 101 nm. Since GA is a kind of Fe(III) ion chelating agent, Fe(III) can be introduced into MoS_2@GA by a chelation reaction to form MoS_2@GA-Fe, which has shown a high therapeutic efficiency.[75]

3.2. Transition metal dichalcogenide-carbon material composites

Carbon materials with excellent photothermal properties are also used to modify TMDs for PTT.[76] Given that heterojunction structure can improve the separation and immigration efficiency of photoexcited charges, researchers often consider utilizing 0D and 2D carbon materials with matched bandgaps to fabricate hybrid heterojunctions which will enhance photothermal conversion performance.[77]

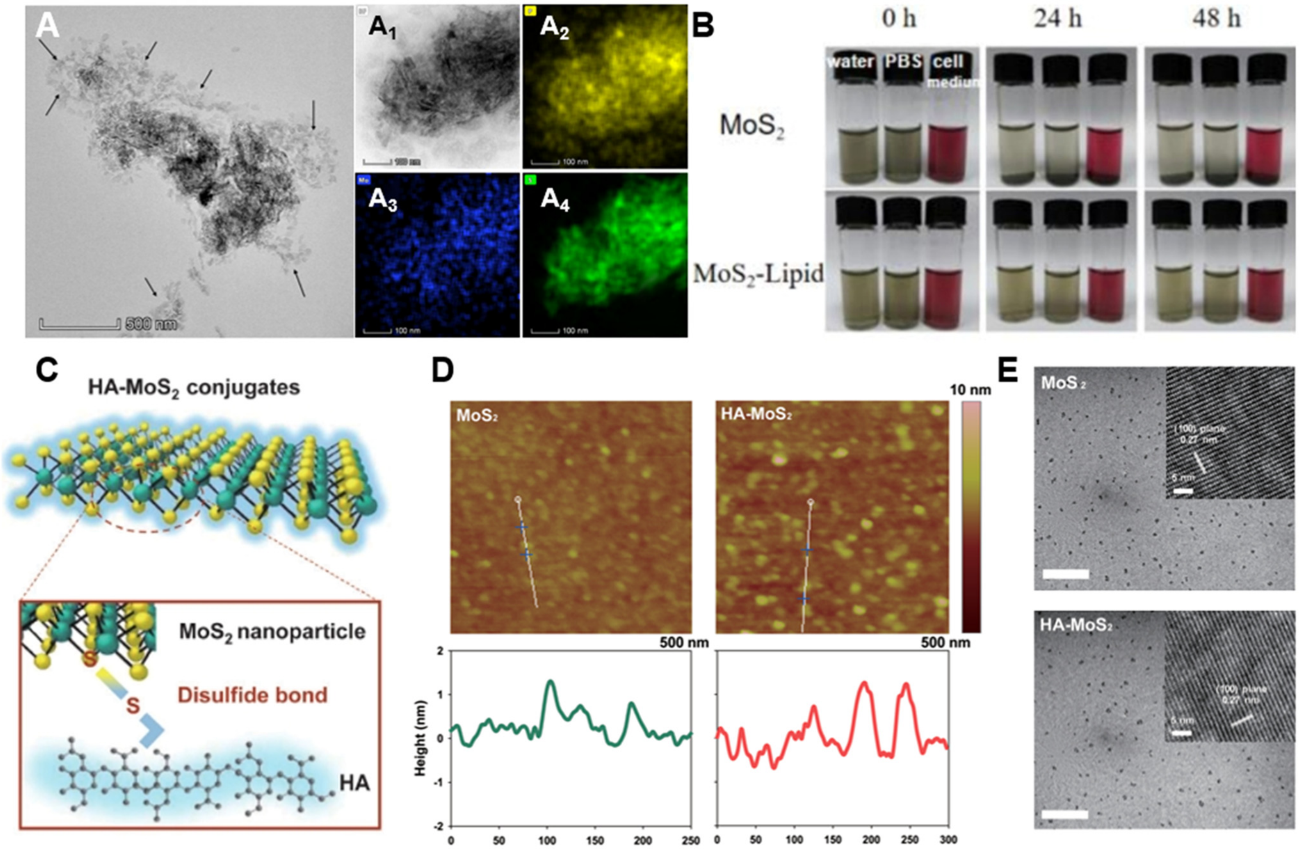

Fig. 4 Preparation and characterization of TMD-organic material composites. (A) Typical TEM image of the MoS_2-lipid. A_1–A_4 are bright-field scanning transmission electron microscopy (BF-STEM) images of the MoS_2-lipid and the corresponding energy dispersive X-ray (EDX) element mappings of P, S, and Mo, respectively. (B) Photographs of MoS_2 (upper) and MoS_2-lipid (bottom) incubated in water, PBS and cell culture medium (containing 10% fetal bovine serum) for 24 hours and 48 hours.[74] Reproduced with permission from ref. 74. Copyright 2020 Elsevier. (C) Scheme of HA-MoS_2 conjugates. (D) AFM images (upper) and the corresponding height profiles (bottom) of MoS_2 (left) and HA-MoS_2 (right). (E) TEM images of MoS_2 (top) and HA-MoS_2 (bottom) (scale bar = 500 nm). Insets: high-resolution TEM (HRTEM) images of MoS_2 and HA-MoS_2.[36] Reproduced with permission from ref. 36. Copyright 2019 Wiley-VCH.

Geng *et al.* designed carbon dot/WS_2 heterojunctions (CD/WS_2 heterojunctions) as NIR-II (near-infrared region II) agents for PTT of osteosarcoma and bone regeneration.[76] As illustrated in Fig. 5A, the preparation of CD/WS_2 heterojunctions can be divided into three procedures, and the binding between CD and WS_2 was mainly through electrostatic interactions. After CDs with a diameter of approximately 10 nm (Fig. 5B) were attached to the surface of WS_2 (Fig. 5C), the thickness showed a distinguishable increase, whereas the average size did not change. In addition, the CD/WS_2 heterojunctions exhibited improved photothermal properties and stability compared to pure CDs and WS_2, which can be verified in the temperature elevation figure.

In addition to combining with WS_2, Geng *et al.* proposed CD-sensitized MoS_2 nanosheet heterojunctions (NIR-CD/MoS_2 HJs).[77] The preparation procedure can likewise be seen as three steps, which contained the synthesis of NIR-CDs and MoS_2-PEG nanosheets along with the surface charge-driven assembly for a 0D/2D/0D sandwich architecture. Upon loading NIR-CDs, dynamic light scattering analysis showed no obvious changes in the hydrodynamic size, and the photothermal conversion efficiency was proportional to the loading level. It can be observed that the MoS_2 nanosheets were almost wrapped in a layer of NIR-CDs. Such a structure, with a loading level as high as 200%, revealed enhanced photothermal effects.

In another typical example, Nandi *et al.* proposed conjugates composed of WS_2 nanorods and CDs (CD/WS_2 nanorods, Fig. 5D).[78] Followed by the addition of glucose gemini surfactant and probe-sonication; the aggregation in the aqueous solution of NH_2-functionalized WS_2 nanorods clearly disappeared. Subsequently, CDs were covalently attached to the surface of WS_2 *via* carbonized amine residues. As shown in the scanning electron microscopy (SEM) image in Fig. 5E, the material exhibited a rod-shaped structure with a length of a few microns.

3.3. Transition metal dichalcogenide-metal chalcogenide composites

To enhance the anti-cancer efficiency, metal chalcogenides with narrow bandgaps are also chosen for combining with

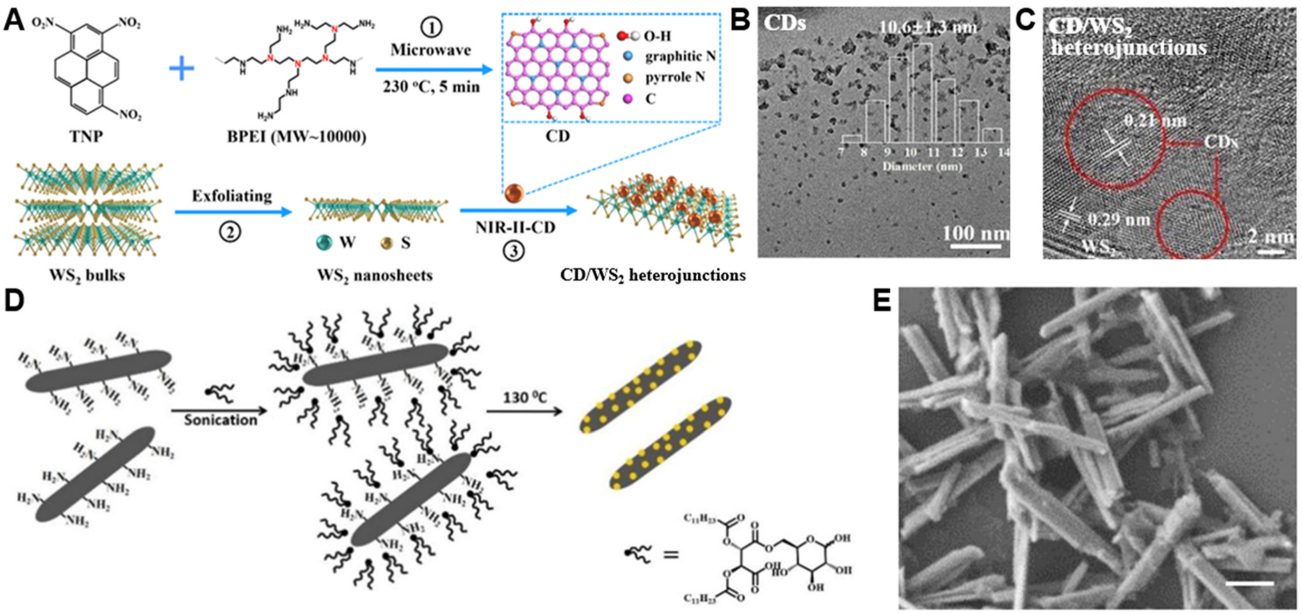

Fig. 5 Preparation and characterization of TMD-carbon material composites. (A) Schematic illustration of the preparation procedures for the CD/WS_2 heterojunctions. (B) TEM image and Gaussian distribution (inset) of NIR-II responsive CDs. (C) HRTEM image of CD/WS_2 heterojunctions.[76] Reproduced with permission from ref. 76. Copyright 2020 Elsevier. (D) Schematic illustration of preparation procedures of CD/WS_2 nanorods. (E) SEM image of CD/WS_2 nanorods (scale bar = 0.5 μm).[78] Reproduced with permission from ref. 78. Copyright 2017 Wiley-VCH.

TMDs.[17] For instance, $Bi_2Se_3/MoSe_2$ nano-heterostructure was successfully constructed by Wang *et al.* for cancer therapy.[17] After preparing $MoSe_2$ nanosheets through ultrasound-assisted exfoliation, the cation-exchange strategy was utilized to partially replace Mo atoms with Bi atoms to form a novel sandwich nanostructure $Bi_2Se_3/MoSe_2/Bi_2Se_3$ (Fig. 6A). As illustrated in Fig. 6B and C, the morphology and size did not change significantly upon the introduction of Bi atoms. To further confirm the crystal structure of $Bi2_{Se}3/MoSe_2/Bi_2Se_3$, selected area electron diffraction (SAED) patterns of $MoSe_2$ and $Bi2_{Se}3/MoSe_2/Bi_2Se_3$ nanosheets were obtained and displayed in Fig. 6D and E, respectively. The additional diffraction spots (Fig. 6E, marked in blue circle) of $Bi2_{Se}3/MoSe_2/Bi_2Se_3$ could be ascribed to the successful exchange between Bi ions and Mo ions. Similarly, Gao *et al.* adopted a one-pot solvothermal protocol to prepare polyvinyl pyrrolidone (PVP)-assisted Bi_2S_3-MoS_2 heterogeneous nanoparticles (BMNPs) as nano-radiosensitizers for triple-negative breast cancer (TNBC).[79] BMNPs presented a uniform morphology and clear crystal structure with an orderly arrangement of lattice fringes.

In another study, Li *et al.* synthesized $MoSe_2/CoSe_2$@PEG nanosheets *via* a one-pot co-deposition strategy for NIR-enhanced chemodynamic therapy (CDT) (Fig. 6F),[80] in which Co-doping enhanced NIR harvesting. As shown in Fig. 6G, the size of the as-prepared $MoSe_2/CoSe_2$ nanosheets was close to 30–50 nm. In addition, the corresponding HRTEM image (Fig. 6H) can confirm the crystal structure of $MoSe_2/CoSe_2$ as it revealed typical lattice fringes of $MoSe_2$ and $CoSe_2$, matching well with the SAED pattern displayed in Fig. 6I. The well distribution of Co, Mo and Se elements in the sample was confirmed by elemental mapping analysis (Fig. 6J).

3.4. Transition metal dichalcogenide-metal composites

Metal nanostructures (*e.g.*, Au and Pt) have unique surface plasmon resonances, and their decorations of semiconductor TMDs are also considered to be good candidates for cancer therapy.[81–83] In a typical example reported by Maji *et al.*, gold nanobipyramids (Au NBPs, right image of Fig. 7A) with a positive charge were used as a substrate to combine MoS_2 nanosheets with a negative charge *via* a strong electrostatic interaction.[81] As can be clearly seen in Fig. 7B–D, Au NBPs with average lengths and widths of approximately 110 nm and 36 nm, respectively, were successfully coated with a thin layer of MoS_2 nanosheets with a thickness of ~1.5–2 nm. Importantly, Au NBPs endowed the hybrid with excellent peroxidase properties and impressive NIR absorbance.

Su *et al.* constructed a colorimetric sensor depending on highly catalytic gold nanoparticle-decorated MoS_2 nanocomposites (MoS_2-AuNPs, Fig. 7E).[84] It can be observed from Fig. 7F and G that the prepared MoS_2 nanosheets showed typical layered nanostructure and Au nanoparticles deposited uniformly on the surface. The UV-*vis* analysis was revealed in Fig. 7H, a new characteristic absorption peak belonged to Au nanoparticles can be observed at 538 nm in MoS_2-AuNPs, which could further confirm the successful synthesis of the nanocomposites. Moreover, the inset in Fig. 7H revealed the difference in color between MoS_2 nanosheets and MoS_2-AuNPs nanocomposites. Owing to the high catalytic activity of MoS_2-AuNPs, researchers have further combined anti-CEA (Ab1, Ab1-

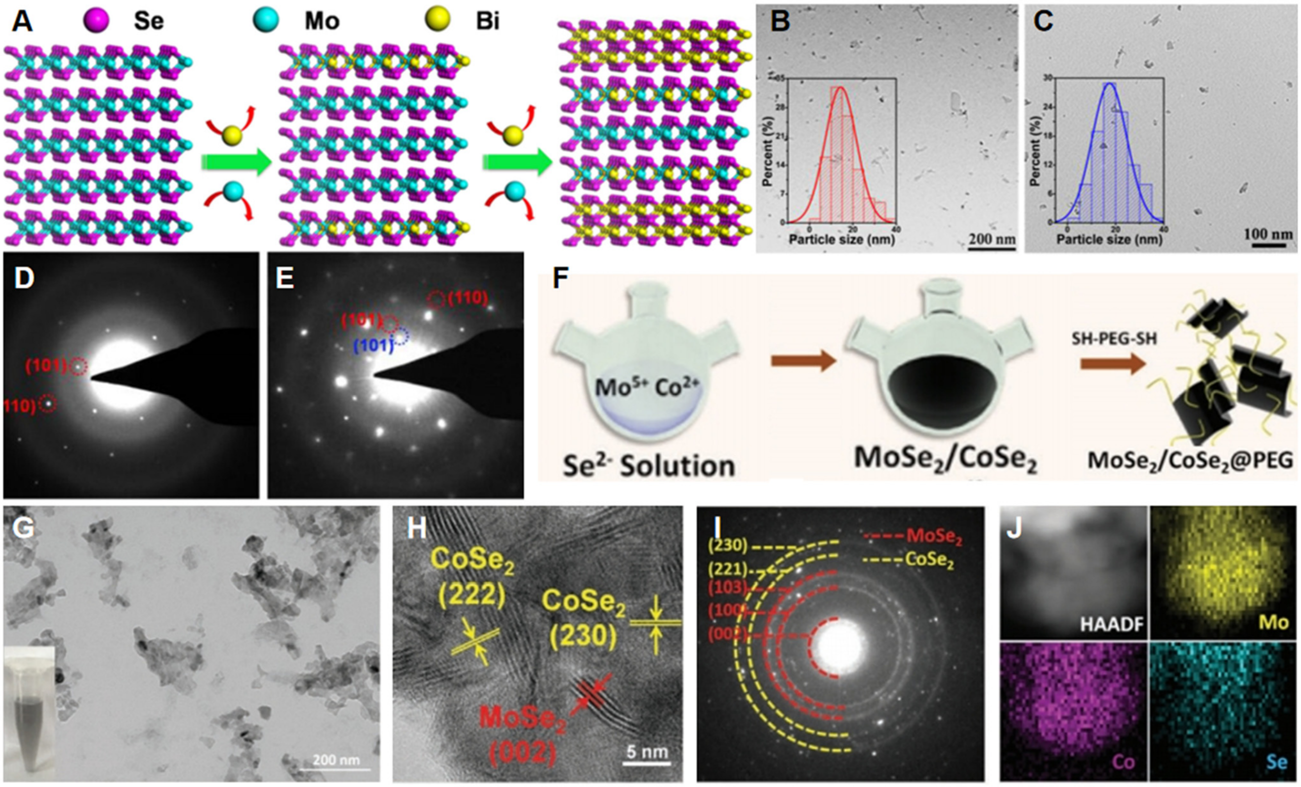

Fig. 6 Preparation and characterization of TMD-metal chalcogenide composites. (A) Side view of cation exchange during the preparation of Bi_2Se_3/$MoSe_2$/Bi_2Se_3 nanostructures. TEM images of (B) $MoSe_2$ and (C) Bi_2Se_3/$MoSe_2$/Bi_2Se_3. SAED patterns for (D) $MoSe_2$ and (E) Bi_2Se_3/$MoSe_2$/Bi_2Se_3.[17] Reproduced with permission from ref. 17. Copyright 2019 Elsevier. (F) Schematic illustration of synthesis of $MoSe_2$/$CoSe_2$@PEG nanosheets. (G) TEM, (H) HRTEM, and (I) SAED images of $MoSe_2$/$CoSe_2$ nanocomposites. Inset: $MoSe_2$/$CoSe_2$ aqueous dispersion. (J) High-angle annular dark-field scanning transmission electron microscopy (HAADF-STEM) image and elemental mapping images of Mo, Se, and Co, respectively.[80] Reproduced with permission from ref. 80. Copyright 2020 Wiley-VCH.

MoS_2-AuNPs) or anti-CEA (Ab2, Ab2-MoS_2-AuNPs) for the diagnosis of cancer (Fig. 7E).

Apart from Au, other metals, *e.g.*, Pt, were also utilized for modifying TMDs.[85–87] For example, Meng *et al.* doped Pt nanoparticles on $MoSe_2$ nanoflowers for synergistic cancer therapies.[86] With the loading of Pt, the shape of $MoSe_2$ was not significantly affected along with their size, which could be verified by corresponding TEM images and dynamic light scattering analysis. Furthermore, it could be observed that Pt nanoparticles uniformly distributed on the surface of $MoSe_2$.

3.5. Transition metal dichalcogenide-oxide composites

In addition, many attempts have been made to combine TMDs with various types of oxides.[88,89] For example, to overcome the limited efficiency of the Fenton-like reaction in CDT, Pidamaimaiti *et al.* functionalized MoS_2 with Cu_2O (Cu_2O-MoS_2) for synergistic CDT and PTT against tumor cells.[88] In which MoS_2 nanosheets were first obtained through a facile solvothermal method, after which Cu_2O nanoparticles were decorated on the surface of MoS_2 nanosheets by electrostatic interactions (Fig. 8A). As presented in Fig. 8B and C, the average size of the nanosheets increased after introducing Cu_2O. As shown in Fig. 8D, Mo, S, Cu, and O coexist and are distributed homogeneously in Cu_2O-MoS_2. Notably, the Cu^+ in Cu_2O can easily react with H_2O_2 to form highly toxic $^{\bullet}OH$, which can strongly promote the Fenton-like reaction in a weakly acidic environment.

In another case, Chen *et al.* introduced ultra-small MoS_2 nanodots to incorporate in mesoporous silica nanospheres (UsMSND@MSN, Fig. 8E) since mesoporous silica nanomaterials are promising candidates for intelligent drug delivery platforms against tumors.[89] As can be seen in Fig. 8F, the uniformed nanosphere structure of UsMSND@MSN was distinguished displayed. Additionally, the dot-like surface of the prepared material was rough with ordered mesopores (Fig. 8G), suggesting the homogeneous incorporation of ultrasmall nanodots in the MSN. UsMSND@MSN remained uniform in size (~115 nm) and biocompatibility, which is in favor of its use as a carrier for anti-cancer drugs.

3.6. Transition metal dichalcogenide-based ternary and multinary compounds

Although so many types of individual materials are mentioned above to modify TMDs, the most common ones are actually TMD-based ternary and multinary compounds.[52] For instance, Li *et al.* developed an anti-cancer drug carrier using MoS_2

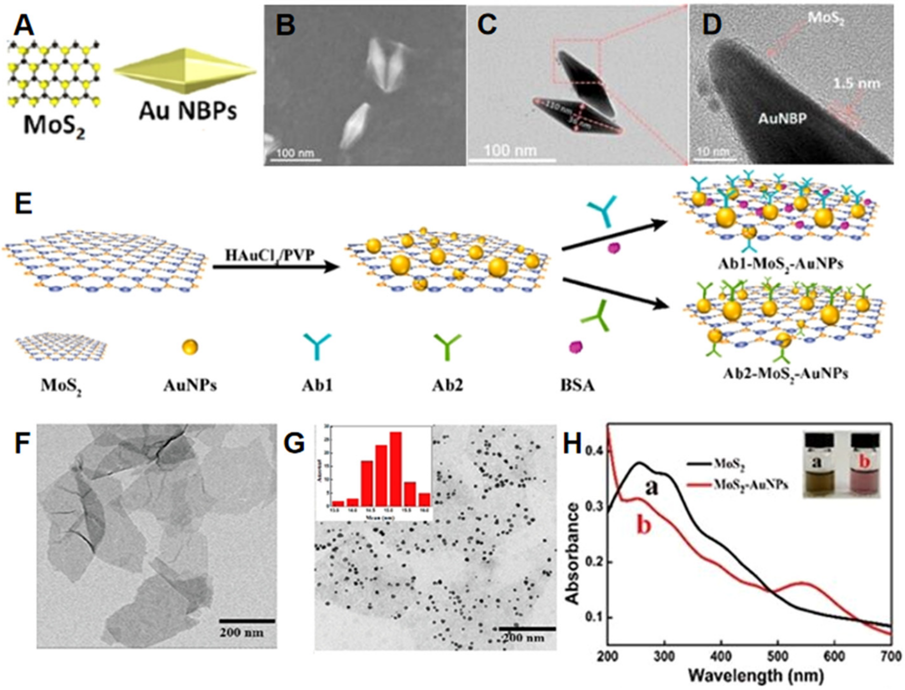

Fig. 7 Preparation and characterization of TMD-metal composites. (A) Structural sketches of MoS$_2$ and Au NBPs. (B) Field-emission SEM (FESEM), (C) TEM, and (D) HRTEM images of AuNBPs@MoS$_2$.[81] Reproduced with permission from ref. 81. Copyright 2018 American Chemical Society. (E) Schematic illustration of the preparation of MoS$_2$-AuNPs and Ab-MoS$_2$-AuNPs nanoprobes. TEM images of (F) MoS$_2$ nanosheets and (G) MoS$_2$-AuNPs nanocomposites. Inset: statistical data on the diameter of AuNPs. (H) Ultraviolet–visible (UV-vis) spectra of MoS$_2$ (a, black line) and MoS$_2$-AuNPs (b, red line). Inset: photos of MoS$_2$ and MoS$_2$-AuNPs.[84] Reproduced with permission from ref. 84. Copyright 2019 American Chemical Society.

modified with lipoic acid (LA)-polyethyleneimine and LA-PEG (MoS$_2$-PEI-PEG, MPP) to combine chemotherapy, gene therapy and PTT.[34] To obtain the well-dispersed products with flake-like shapes, the heating time during the hydrothermal process for preparing MoS$_2$ nanosheets was chosen to be 10 hours. Because the sulfur molecules in LA would bind to the defects of MoS$_2$, the LA-dominated thiol reaction could help couple PEI and PEG to the nanosheets. The TEM image obtained after coupling clearly demonstrated that the flake-like structure did not change and the core–shell structure appeared. As PEI and PEG are both hydrophilic, they were also proven to clearly improve the colloidal stability and dispersion of MoS$_2$ nanosheets.

Mussel-inspired chemistry, which takes advantage of polydopamine (PDA), provides another novel surface-modification strategy. Zeng *et al.* prepared MoS$_2$ nanosheets modified with PDA and poly((polyethylene glycol) methyl ether methacrylate) (PPEGMA) (MoS$_2$-PDA-PPEGMA) through mussel-inspired chemistry along with chain transfer free radical polymerization to conquer cancer, in which MoS$_2$ nanosheets were synthesized *via* lithium intercalation exfoliation.[90] It can be observed from TEM images that the thickness of the obtained nanocomposites significantly increased due to the successful coating of PDA thin films and PPEGMA on the surface of MoS$_2$.

To study the efficacy of rod-shaped MoS$_2$-based nanoplatform for PTT, Yang *et al.* synthesized MoS$_2$ nanosheets coated with mesoporous silica nanorods (MSNR) along with human serum albumin (HSA) modifying and chlorin e6 (Ce6) loading (MSNR@MoS$_2$-HSA/Ce6).[33] Utilizing silica nanorods as templates, MSNR@MoS$_2$ were prepared through a facile hydrothermal method. Moreover, HSA, which is defined as an endogenous protein, and Ce6, a hydrophobic photosensitizer, were introduced into MSNR@MoS$_2$ nanocomposites for more accurate targeted tumor therapy under NIR irradiation (Fig. 9A). As presented in TEM images (Fig. 9B and C), MSNR@MoS$_2$ displayed obscurer edges compared to pristine MSNR. Interestingly, MSNR@MoS$_2$-HSA exhibited smoother edges than MSNR@MoS$_2$. Furthermore, the loading of Ce6 could be verified by the existing quenching effect, as a new characteristic peak at 404 nm appeared in the UV-*vis* spectra of MSNR@MoS$_2$-HSA/Ce6, whereas MSNR@MoS$_2$-HSA did not. These results confirmed the successful realization of each procedure.

3.7. Others

There are also several other types of materials that have been used for surface functionalization of TMDs.[91] For instance, rare earth element-based upconversion nanoparticles (UCNPs), which are considered difficult to combine with effective photothermal therapeutic materials into a small-sized structure. Wang *et al.* grew VS$_2$ directly on the surface of luminescent UCNPs to obtain oil-soluble UCNPs@VS$_2$ nanocomposites and

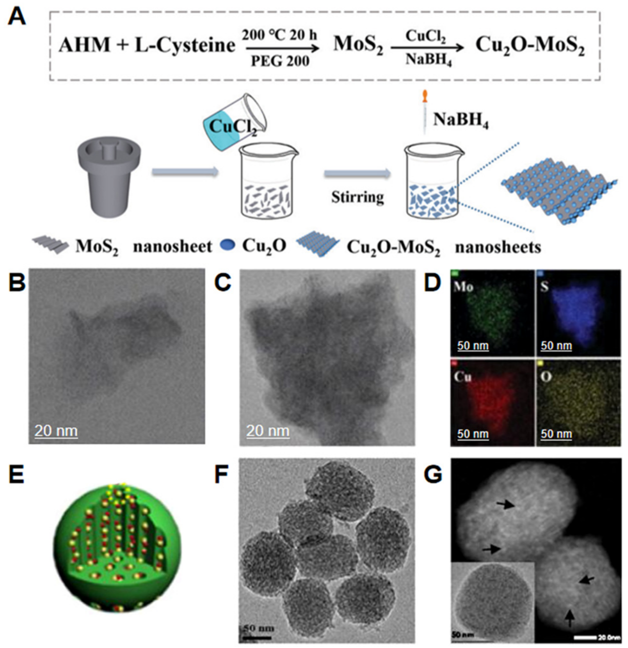

Fig. 8 Preparation and characterization of TMD-oxide composites. (A) Schematic illustration of the synthesis of Cu_2O-MoS_2 nanosheets. TEM images of (B) MoS_2 and (C) Cu_2O-MoS_2. (D) Elemental mapping images of Mo, S, Cu, and O.[88] Reproduced with permission from ref. 88. Copyright 2021 Royal Society of Chemistry. (E) Structural sketch, (F) TEM, and (G) STEM images of UsMSND@MSN. Inset: enlarged TEM image of an individual UsMSND@MSN nanoparticle.[89] Reproduced with permission from ref. 89. Copyright 2021 Elsevier.

then modified them with PEG (mPEG) for better water solubility (UCNPs@VS_2-mPEG).[91] Such nanostructure provides an effective strategy for integrated materials based on UCNPs assessing nanoscale dimension. As illustrated in Fig. 10A, $NaYF_4$:Yb,Tm@$NaGdF_4$ (UCNPs) exhibited a core–shell structure, and UCNPs@VS_2-mPEG was synthesized successfully. TEM images presented in Fig. 10B–D verified the integration of VS_2 and mPEG with UCNPs, which was consistent with the results of elemental mapping images. Besides, growing VS_2 on the surface of UCNPs did not influence the average size (~25 nm) of nanocomposites.

In another case, Zhao *et al.* proposed LDH-MoS_2 (LMM) clay nanosheets for cancer therapy. Beyond that, bovine serum albumin (BSA) was modified on the surface of LMM to improve the colloidal stability and biocompatibility of materials in both vitro and vivo together with Ce6, which acted as a photosensitizer beneficial for enhancing therapeutic efficacy (LMM@BSA/Ce6, Fig. 10E).[16] It can be observed from SEM images (Fig. 10F) and TEM images (Fig. 10G) that LMM@BSA showed 2D structure as well as LMM.

3.8. Structure of transition metal dichalcogenide-based composites

TMD-based composites can be divided into four categories according to their structure: 0D/2D, core–shell, 2D/2D, and inorganic–organic. A scheme of the 0D/2D structure is shown in Fig. 11A, where 0D nanoparticles are explicitly embedded in

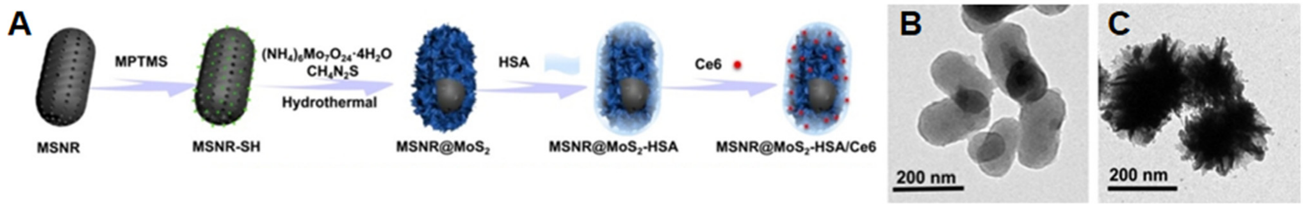

Fig. 9 Preparation and characterization of TMD-based ternary and multinary compounds. (A) Schematic illustration of the preparation of MSNR@MoS_2-HSA/Ce6. TEM images of (B) MSNR and (C) MSNR@MoS_2.[33] Reproduced with permission from ref. 33. Copyright 2019 Ivyspring International Publisher.

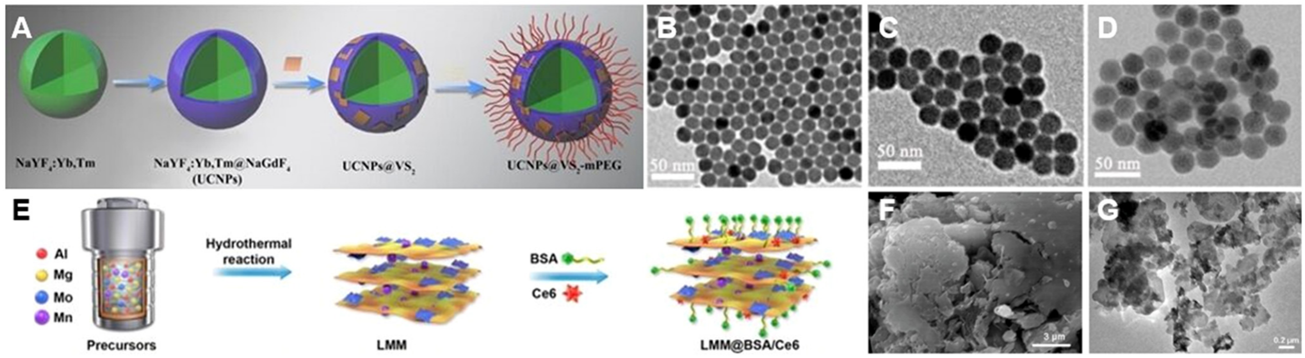

Fig. 10 Preparation and characterization of TMD-other material composites. (A) Schematic illustration of the preparation of UCNPs@VS_2-mPEG nanostructure. TEM images of (B) UCNPs, (C) UCNPs@VS_2, and (D) UCNPs@VS_2-mPEG.[91] Reproduced with permission from ref. 91. Copyright 2020 Royal Society of Chemistry. (E) Schematic illustration of the synthesis procedure of LMM@BSA/Ce6 nanosheets. (F) SEM image of LMM nanosheets and (G) TEM image of LMM@BSA.[16] Reproduced with permission from ref. 16. Copyright 2021 BioMed Central.

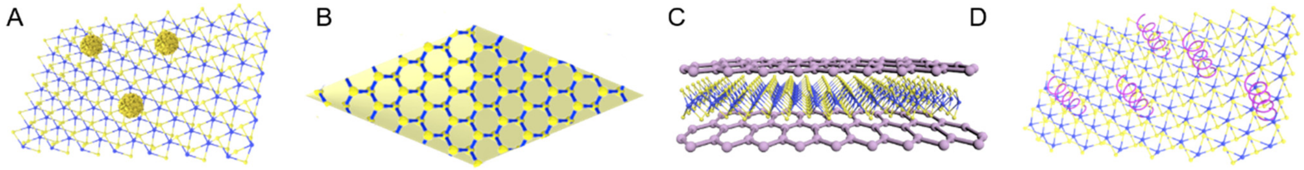

Fig. 11 Structure of TMD-based composites. Schematic diagrams of (A) 0D/2D, (B) core–shell, (C) 2D/2D, and (D) inorganic–organic structures.

2D nanosheets. The adsorption of CDs on WS_2 nanosheets (CD/WS_2) is a typical example of 0D/2D structures. Through electrostatic interactions, CD/WS_2 nanocomposites with excellent photothermal effects and physiological stability were synthesized, which could be used for PTT against tumors.[76] Fig. 11B shows a schematic diagram of the core–shell structure with the characterization that one material coats on another material. AuNBPs@MoS_2 fabricated by Maji *et al.* had such a core–shell structure, and it exhibited excellent photothermal effects that were efficient for anti-cancer treatment.[81] The 2D/2D structure is an alternative type of representative structure as well. Wang *et al.* successfully combined NIR-CDs with MoS_2 nanosheets to synthesize NIR-CD/MoS_2 heterojunctions with a 2D/2D structure (Fig. 11C). During the preparation, ultrasonic exfoliation and cation exchange were the main preparation procedures, and the products had a high surface area to volume ratio along with superior photothermal performance.[77] Although the aforementioned structures have terrific NIR absorption energy for cancer therapy, their poor biocompatibility would limit the corresponding development to some extent. To address this issue, Yi *et al.* proposed an organic–inorganic structure (Fig. 11D) *by* encapsulating ultrathin WS_2 nanosheets with BSA. Through 3-(4,5-dimethylthiazol-2-yl)-2,5-diphenyltetrazolium bromide (MTT) assay and zebrafish embryo survival rate experiment, this organic–inorganic structure displayed excellent biocompatibility.[92]

4. Synthesis of transition metal dichalcogenide-based composites

Synthesis strategies for TMD-based composites generally involve hydrothermal/solvothermal methods[15,79] and surface deposition/coating.[93,94] In this section, we focus on the typical synthetic strategies for TMD-based composites.

4.1. Hydrothermal/solvothermal methods

Hydrothermal/solvothermal methods are commonly employed to prepare TMD-based composites with high crystallinity, thanks to their cost-effectiveness and simple operational procedures[95,96] As displayed in Fig. 12A, such Fe(III)@WS_2-PVP nanocapsules[87] were prepared *via* a one-pot solvothermal method by Wu *et al.*, in which WS_2 nanosheets and Fe(III) species were transformed from ammonium tetrathiotungstate ($H_8N_2S_4W$) and ferric chloride hexahydrate ($FeCl_3 \cdot 6H_2O$), respectively. During the preparation process, a plentiful inner space in nanocapsules formed because the Fe(III) species would roll up the WS_2 nanosheets, which could lead to an improved drug loading capacity of Fe(III)@WS_2-PVP. Moreover, the modification of PVP on the surface of nanocapsules has been demonstrated to greatly enhance their colloidal stability and biocompatibility. The SEM image in Fig. 12B shows the successful synthesis of Fe(III)@WS_2-PVP, and the red arrows indicate the Fe(III) species.

Moses O. A. *et al.* produced PVP intercalated metallic 1T-WSe_2 nanosheets (1T-WSe_2@PVP) *via* a one-step solvothermal approach as well.[97] During the preparation, *N*,*N*-dimethylformamide (DMF) solvent was also utilized for the dissolution of materials which contained 0.5 mmol selenourea powder, 0.1 mmol WCl_6, and 0.5 g PVP. The as-prepared solution was then transferred into a sealed autoclave and heated at 220 °C for 24 hours. It can be seen from the SEM image that the obtained 1T-WSe_2@PVP exhibited a uniform nanosheet structure. Additionally, such ultrathin nanosheets consisted of 3–8 layers which can be confirmed by the high-magnification TEM image.

Likewise, Wang *et al.* proposed a PVP-mediated hydrothermal reaction to prepare WS_2-$PVP_{360\ kDa}$ (the weight average molecular weight of PVP is 360 kDa) nanosheets (Fig. 12C), and it could achieve synthesis and surface modification at the same time.[51] During the synthesis process, 0.15 g $(NH_4)_2WS_4$ served as a source of S and W elements while 0.15 g PVP was selected as a modifier. A homogeneous solution was obtained by dissolving $(NH_4)_2WS_4$ and PVP in 30 mL of DMF with vigorous magnetic stirring. The as-obtained solution was then transferred into a 100 mL stainless-steel autoclave lined with polyphenylene and heated at 220 °C for 12 hours. The final products are displayed in Fig. 12D, and a uniform and regular disk shape with a nanosheet morphology can be observed clearly.

In another typical example, Mao *et al.* adopted a one-pot hydrothermal synthesis to prepare $MoSe_2$ hetero-dimensional hybrid which was self-assembled by $MoSe_2$ nanodots and small-sized $MoSe_2$ nanosheets (Fig. 12E).[98] Na_2MoO_4 and Se were utilized as precursors and PEG served as the capping agent. Furthermore, a solution with a Mo : Se molar ratio of 1 : 2 was transferred into an 80 mL autoclave lined with Teflon and then heated at 200 °C for 12 hours. As can be observed from TEM images, the obtained $MoSe_2$ hetero-dimensional hybrid had a flake-like structure. Moreover, large amounts of evenly sized $MoSe_2$ nanodots were dispersed on the surface of the $MoSe_2$ nanosheets (Fig. 12F). Such phenomenon above could be well explained by the capping effect of PEG.

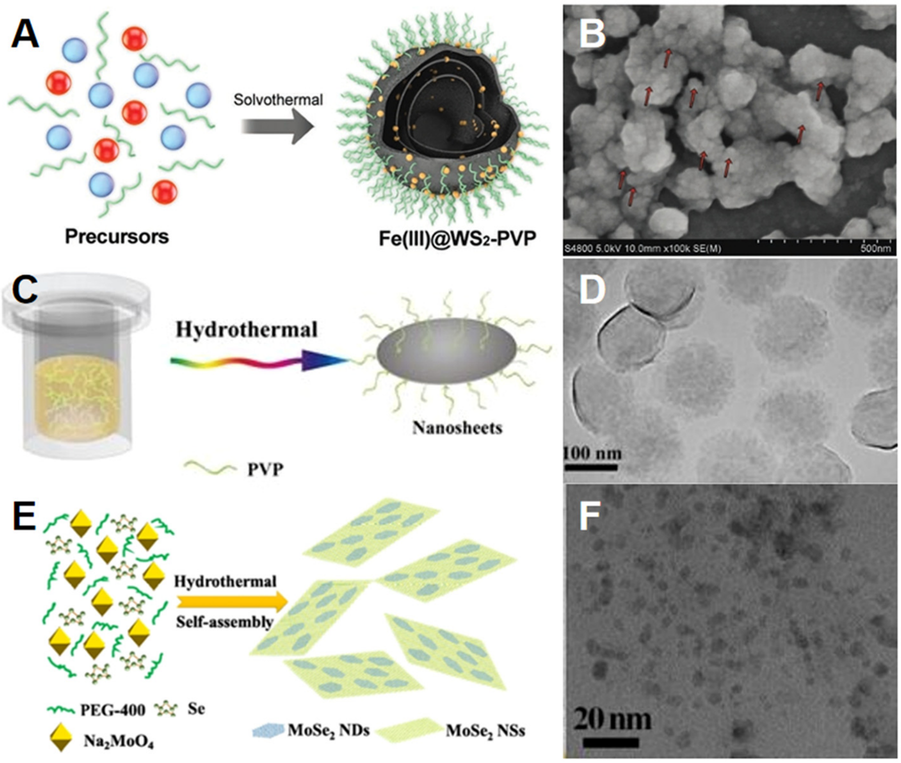

Fig. 12 Hydrothermal/solvothermal methods for preparing TMD-based composites. (A) Schematic illustration of the solvothermal synthesis of Fe(III)@WS_2-PVP nanocapsules. (B) SEM image of Fe(III)@WS_2-PVP nanocapsules.[87] Reproduced with permission from ref. 87. Copyright 2019 Wiley-VCH. (C) Schematic illustration of the hydrothermal synthesis of WS_2-PVP nanosheets. (D) TEM image of WS_2-$PVP_{360\ kDa}$ nanosheets.[51] Reproduced with permission from ref. 51. Copyright 2017 Elsevier. (E) Schematic illustration of hydrothermal synthesis of $MoSe_2$ hetero-dimensional hybrid. (F) TEM image of the $MoSe_2$ hetero-dimensional hybrid.[98] Reproduced with permission from ref. 98. Copyright 2017 Tsinghua University Press.

4.2. Surface deposition/coating

Some materials, like organic compounds, are commonly combined with TMDs using surface deposition/coating techniques. These methods provide better control over preparation parameters, enabling faster reaction times.[99,100] Wang *et al.* coated PEG on the surface of $MoSe_2$ nanoflowers ($MoSe_2$@PEG), which could be served as an efficient nanoplatform for drug loading and delivery.[101] The target product $MoSe_2$@PEG was obtained by dispersing 20 mg prepared $MoSe_2$ nanoflowers into PEG5000-NH_2 aqueous solution (1 mg mL^{-1}, 5 mL), followed by ultrasonication for 4 hours. Subsequently, the anticancer drug, Doxorubicin (DOX), could be loaded onto $MoSe_2$@PEG for cancer therapy ($MoSe_2$@PEG-DOX). From Fig. 13A and B, it can be clearly observed that the nanocarrier was successfully synthesized with the introduction of PEG and DOX. Additionally, PEG enhanced the stability and biocompatibility of the obtained compositions.

In addition to organic materials, metal ions have also been used to dope TMDs *via* a surface deposition approach.[102,103] Pan *et al.* utilized a facile liquid-phase strategy to synthesize Gd^{3+}-doped $MoSe_2$ nanosheets ($MoSe_2(Gd^{3+})$) as a cancer therapeutic agent and a contrast agent.[104] To enhance the stability in physiological solutions, PEG was modified on the surface of $MoSe_2(Gd^{3+})$ ($MoSe_2(Gd^{3+})$-PEG, Fig. 13C). During the preparation process, Gd^{3+} ions were introduced into $MoSe_2$ crystals by adding anhydrous ethanol with gadolinium chloride to a beaker containing 25 mL distilled water along with 1.645 g $NaMoO_4·2H_2O$, 1.549 g Se, 0.259 g $NaBH_4$, and $GdCl_3·6H_2O$. Besides, *N*-methyl-2-pyrrolidone could assist the exfoliation of MoSe2 nanosheets from bulk $MoSe_2$. As shown in Fig. 13D, the obtained $MoSe_2(Gd^{3+})$ exhibited a sheet structure. From Fig. 13E, the AFM image well displays the doping of Gd^{3+} into the crystals.

5. Application for cancer treatments

As the incidence and mortality rates of cancer continue to rise in recent years,[105,106] researchers have explored many nanomaterials for tumor treatment, including lung cancer, prostate cancer, and breast cancer *et al.*[29,107,108] Among them, TMD-based composites have been gradually developed and used for effective tumor elimination[109,110] by virtue of their good photothermal conversion efficiency,[35] excellent biocompatibility[33] and large specific surface area.[111] In this section, we will elaborate on the application of TMD-based composites for cancer treatments.

5.1. Chemotherapy

Chemotherapy, a widely applied anti-cancer strategy, often uses chemically synthesized drugs (*e.g.*, DOX) to treat tumor tissues. It functions by interfering with DNA and RNA in cells

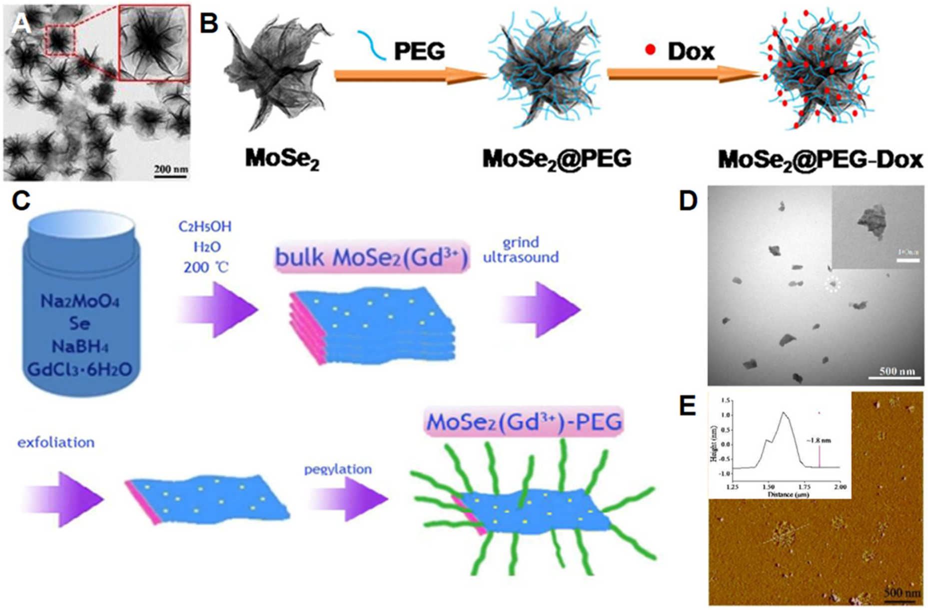

Fig. 13 Surface deposition/coating for preparing TMD-based composites. (A) TEM image of $MoSe_2$ nanoflowers. (B) Schematic illustration of the preparation process of $MoSe_2$@PEG-DOX nanocomposites.[101] Reproduced with permission from ref. 101. Copyright 2018 Royal Society of Chemistry. (C) Schematic illustration of the synthesis process of $MoSe_2(Gd^{3+})$-PEG. (D) TEM image of $MoSe_2(Gd^{3+})$ nanosheets. Inset: Magnified TEM image of an individual $MoSe_2(Gd^{3+})$ nanosheet. (E) AFM image of $MoSe_2(Gd^{3+})$ nanosheets. Inset: thickness profile of $MoSe_2(Gd^{3+})$ nanosheets.[104] Reproduced with permission from ref. 104. Copyright 2018 Royal Society of Chemistry.

or proteins to inhibit the growth of cancer cells. However, such treatment still suffers from some problems like instability, poor solubility, and inefficiency of chemotherapeutic agents due to the non-specific uptake of cancer cells, which will result in distinct side effects. Therefore, 2D TMD-based composites, which can be excellent drug carriers, play an important role in reducing side effects and boosting the anti-cancer effects of chemotherapy.

Li *et al.* successfully prepared MoS_2 superstructures (layer-by-layer (LbL)-DNA/MoS_2 nanosheets) through the rapid self-assembly of complementary DNA oligonucleotides anchored on MoS_2 nanosheets to load DOX (DOX/DNA/MoS_2).[112] Specifically, DNA can bind to the surface of MoS_2 through interactions between its thiol groups and sulfur vacancies in MoS_2, allowing doxorubicin (DOX) to intercalate within the DNA duplex. In the presence of adenosine triphosphate (ATP), a crucial metabolic coenzyme, the DNA/MoS_2 complex responds by disassembling, triggering the controlled release of DOX. This ATP-sensitive mechanism facilitates targeted chemotherapy by ensuring drug release primarily in tumor regions, where ATP concentrations are higher (Fig. 14A). Additionally, DNA anchoring markedly prevented the aggregation of MoS_2 in the physiological environment, which enhanced its stability and drug delivery efficiency. To investigate the biodegradability of DOX-loaded DNA/MoS_2 during tumor cell killing, DOX/DNA/MoS_2 nanosheets were exposed to DNAase, and the MoS_2 nanosheets effectively protected DNA from degradation, indicating the excellent biocompatibility of DNA/MoS_2 nanosheets. As expected, this composite ultimately demonstrated the optimal tumor-suppressing effect, and its high degree of inertness protected DNA from enzymatic cleavage until it entered ATP-rich cancer cells, obviously enhancing the targeted DOX release from chemotherapy.

Beyond that, Dong *et al.* presented a PEI-assisted MoS_2 modified with hyaluronic acid (MoS_2-PEI-hyaluronic acid) and loaded DOX to combat chemoresistance in clinical oncology, where PEI was introduced by electrostatic interaction and the –COOH of hyaluronic acid was coupled with the $-NH_2$ of PEI.[113] Hyaluronic acid, a biocompatible polysaccharide, is specifically broken down by hyaluronidase, an enzyme mainly found in the tumor microenvironment and lysosomes. This controlled degradation helps maintain MoS_2 stability in aqueous and physiological conditions, facilitating targeted tumor therapy. After investigating the DOX release ability of MoS_2-PEI-hyaluronic acid at tumor sites under different pH and laser irradiation conditions, the DOX cumulative release rate of MoS_2-PEI-hyaluronic acid was calculated to be as high as 77.4% under acidic conditions along with low-power density NIR laser irradiation due to the multi-stimuli-accelerated release of DOX and the improved accumulation of DOX depending on the downregulation of the expression of drug-resistance-related proteins in the tumor microenvironment. *In vivo* experiments showed that mice bearing tumors did not experience significant weight loss, but exhibited a substantial decrease in tumor volume under 808 nm NIR laser radiation, confirming that MoS_2-PEI-hyaluronic acid had excellent biocompatibility (Fig. 14B) and the ability to overcome drug resistance issues in chemotherapy (Fig. 14C).

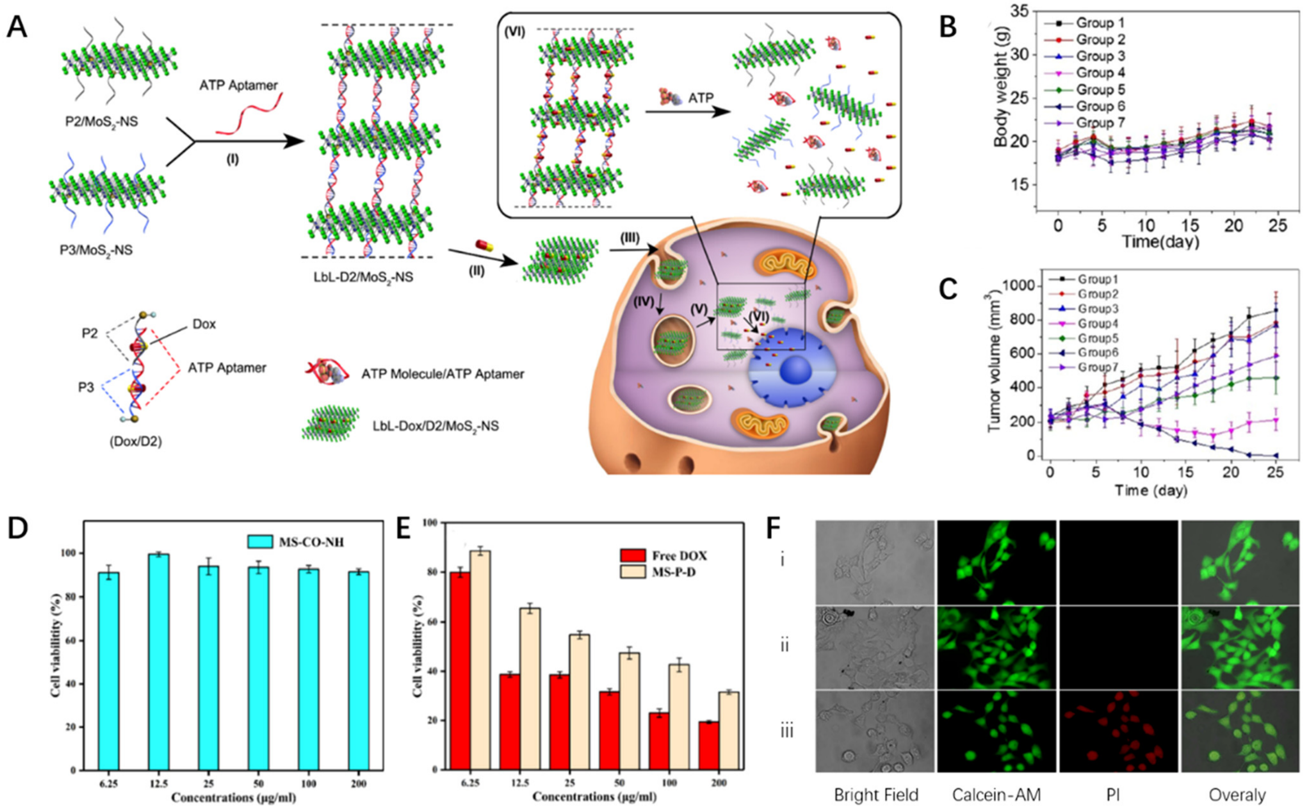

Fig. 14 TMD-based composites for chemotherapy. (A) Schematic illustration of the chemotherapy mechanism of multilayer DOX/DNA/MoS_2 nanosheets.[112] Reproduced with permission from ref. 112. Copyright 2017 American Chemical Society. (B) Body weight curves of mice in each group. (C) Tumor volume curves after 25 days of treatment in each group. (group 1: saline; group 2: saline + NIR; group 3: MoS_2-PEI-HA; group 4: free DOX; group 5: MoS_2-PEI-HA + NIR; group 6: DOX@MoS_2-PEI-HA; group 7: DOX@MoS_2-PEI-HA + NIR)[113] Reproduced with permission from ref. 113. Copyright 2018 American Chemical Society. (D) Cell viabilities of human hepatocellular carcinomas (HepG2) cells treated with different concentrations of MS-CO-NH. (E) Cell viabilities of HepG2 cells treated with different concentrations of MS-P-D and free DOX.[114] Reproduced with permission from ref. 114. Copyright 2020 Royal Society of Chemistry. (F) The live/dead cell images of HaCaT cells stained with Calcein AM and PI after various treatments of (i) control, (ii) TGA-WS_2-PPy-Fu nanocomposite, and (iii) drug-released solution from TGA-WS_2-PPy-FU.[115] Reproduced with permission from ref. 115. Copyright 2020 Elsevier.

Apart from these examples, Long *et al.* synthesized a pH-responsive drug delivery system through a straightforward approach for chemotherapy.[114] They employed lithium-ion-assisted liquid-phase exfoliation to prepare multilayered nanoparticles, and the surface defects were modified with aldehyde-PEG (CHO-PEG) and thiolated methoxypolyethylene glycol to enhance the dispersibility, stability, and pH responsiveness. An anti-cancer drug, DOX, was then loaded onto the surface of nanoparticles (MoS_2-PEG-DOX, MS-P-D) *via* a pH-responsive oxime chemical bond (MoS_2-carbonyl-imino, MS-CO-NH) formed between the carbonyl group of CHO-PEG and the amine group of DOX. To evaluate the effectiveness of this system in eliminating cancer cells, MTT assays were conducted, which revealed the excellent biocompatibility of MS-CO-NH (Fig. 14D), along with the highest rate of DOX release under acidic conditions. Moreover, when tumor cells were co-cultured with the MS-P-D composite material, their cell viability significantly decreased (Fig. 14E), indicating that the capacity of MS-P-D to kill cancer cells was comparable to that of high concentrations of free DOX.

In a separate study, Hsiao *et al.* developed a novel drug delivery carrier, thioglycolic acid-WS_2-polypyrrole-5-fluorouracil (TGA-WS_2-PPy-FU), which utilized electrical stimulation for drug release.[115] The incorporation of PPy, a representative polymer, enhanced the sensitivity to electrical stimuli, thereby improving drug delivery. To study the efficacy of TGA-WS_2-PPy-FU in cancer treatment, UV-*vis* spectroscopy was employed to monitor drug release and the result showed that such material exhibited the best drug release behavior under electrical stimulation. Subsequently, they assessed the viability of human keratinocyte (HaCaT) cells treated with non-electrically stimulated TGA-WS_2-PPy-FU using an MTT assay, which showed over 80% cell viability, indicating good biocompatibility. Furthermore, calcein acetoxymethyl ester (Calcein AM) and propidium iodide (PI) staining (Fig. 14F) were used for live/dead cell determination, during which TGA-WS_2-PPy-FU exhibited superior biocompatibility and could effectively release chemotherapy drugs under electrical stimulation. Moreover, both drug-loaded- and drug-free-TGA-WS_2-PPy-FU were applied onto patches, which were then affixed to the skin followed by electrical stimulation. Based on the Raman spectroscopy results, TGA-WS_2-PPy-FU was concluded to be the platform with the strongest drug release signal. These findings collectively demonstrate the potential of TGA-WS_2-PPy-FU for application in chemotherapy. Overall, TMD-based composites show non-negligible potential for loading chemical drugs, which significantly improves drug delivery rate and chemotherapeutic efficiency.

5.2. Photothermal therapy

PTT, one of the most promising treatments for tumors, which depends on converting light energy into heat energy, often results in localized hyperthermia that drives the death of cancer cells. It has attracted increasing attention recently thanks to its ability to precisely target lesions with a controllable dose of external laser irradiation, thus minimizing damage to the surrounding healthy tissue. However, pure TMDs lack stability and sometimes exhibit potential side effects, poor photothermal conversion efficiency, and inferior biocompatibility, which limits their clinical medical applications. Consequently, there is an urgent need to exploit TMD-based photothermal agents to address these issues.

For example, Ariyasu *et al.* synthesized a photothermal agent by coating MoS_2 with a thiolated CS. With CS coating, the aggregation of MoS_2 was distinctly prevented, thus the stability and dispersibility of the material in a biological context were enhanced.[116] To inhibit heat shock protein 90 (Hsp90), which helps tumors resist thermal stress, a cyclic peptide sequence (Cype), an Hsp90 inhibitor analog, was loaded onto MoS_2-CS. The addition of CS and Cype had little effect on the thermal properties of composite, preserving its strong photothermal performance. Under 808 nm NIR irradiation, Cype specifically bound to the N-middle domain of Hsp90, disrupting its function and weakening cellular resistance to heat treatment (Fig. 15A). Additionally, the CS modification contributed to better biocompatibility and potential biodegradability, supporting safer therapeutic applications. Besides, experiments with human colon cancer (HCT-116) cells proved that MoS_2-CS-Cype showed more effective PTT efficacy and hypotoxicity (Fig. 15B) compared to pure MoS_2 and MoS_2-CS, which was attributed to the rapid release of Cype and the increase in the photothermally mediated apoptosis.

In another case, Chen *et al.* prepared MoS_2 nanosheets *via* a one-pot hydrothermal method, followed by surface coating with polyethyleneimine hydrochloride and polyacrylic acid (PAH/PAA).[93] Subsequently, an amination reaction between the amino groups of BSA-Gd composite and carboxyl groups of MoS_2 nanosheets yielded MoS_2-Gd-BSA nanosheets. The photothermal effect and stability of the modified MoS_2-Gd-BSA nanosheets were investigated by irradiating them with different laser frequencies and then examining the temperature curves upon repeated irradiation. As a result, BSA-Gd-

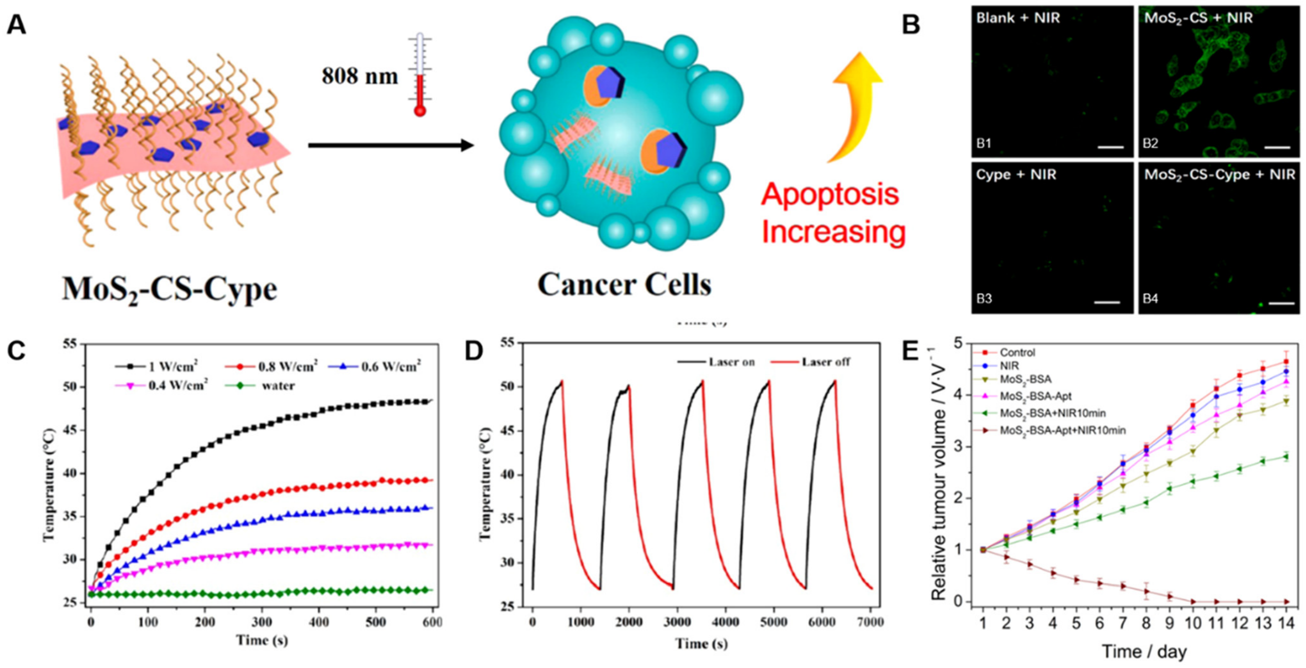

Fig. 15 TMD-based composites for PTT. (A) Schematic illustration of the PTT process-based on MoS_2-CS-Cype. (B) Fluorescence expression images of HCT-116 cells stained by Alexa Flour 488 labeled anti-Hsp70 antibody after various treatments of (B1) NIR only, (B2) MoS_2 + NIR, (B3) Cype + NIR, and (B4) MoS_2-CS-Cype + NIR.[116] Reproduced with permission from ref. 116. Copyright 2017 American Chemical Society. (C) Temperature change curves of 100 μg mL^{-1} MoS_2-Gd-BSA solution under the 808 nm laser at different power densities for 10 minutes. (D) Temperature changes in MoS_2-Gd-BSA as measured by on/off irradiation cycles. (808 nm laser, 50 μg mL^{-1}).[93] Reproduced with permission from ref. 93. Copyright 2017 American Chemical Society. (E) Tumor volume growth changes of tumor-bearing mice under different treatments.[117] Reproduced with permission from ref. 117. Copyright 2021 Elsevier.

MoS_2 displayed a good photothermal effect and stability (Fig. 15C and D). The toxicity of MoS_2-Gd-BSA was also assessed during the cell incubation using the Cell Counting Kit-8 (CCK-8) assay, which revealed that the materials had low toxicity. Encouraged by these conclusions, they conducted *in vivo* experiments on 4T1 (breast cancer) tumor-bearing mouse models and found significant tumor growth suppression under laser irradiation with MoS_2-Gd-BSA treatment, together with no observed tumor recurrence, which suggests its potential for cancer treatments.

To obtain nanostructures with high specificity for tumor cell recognition and effective enrichment at the tumor site, Pang *et al.* synthesized ~10 nm MoS_2 nanosheets by a hydrothermal method, conjugated with BSA and a specific nuclear accounting adapter (Apt) to prepare MoS_2-BSA-Apt nanosheets.[117] Upon examining the physical and chemical properties of the composite, they found that it exhibited outstanding photothermal effect and stability. MoS_2-BSA-Apt was then incubated with MCF-7 human breast cancer cells to assess their survival rate. Consequently, MoS_2-BSA-Apt exhibited low cell toxicity and excellent tumor-targeting capabilities. Given these excellent properties, *in vitro*/vivo experiments were conducted as well, which demonstrated the effective ablation of human breast cancer cells under the treatment of MoS_2-BSA-Apt + NIR 10 min (Fig. 15E). In summary, MoS_2-BSA-Apt has the potential to become a photothermal material for tumor precision treatments.

In summary, TMD-based composites exhibit superior photothermal conversion efficiency and stability, making them outstanding photothermal agents for killing tumor cells. Moreover, compared to gold nanoparticles, TMD-based composites provide a more practical and affordable option for PTT, benefiting from their low material costs and economical synthesis methods.[118–120]

5.3. Phototherapy

Although PTT is effective, to a certain extent, the results of a single therapy are often suboptimal. Therefore, phototherapy, mainly including PTT and photodynamic therapy (PDT), is employed to further enhance the effectiveness of cancer treatments. In phototherapy, phototherapeutic agents absorb visible/NIR light, generating hyperthermia or cytotoxic substances such as reactive oxygen species (ROS), including singlet oxygen ($^1O_2$), superoxide radicals ($^\bullet O_2^{\bullet -}$), and hydroxyl radicals ($^\bullet OH$) to induce cancer cell damage.

In 2019, Younis *et al.* absorbed positively charged Au nanorods onto negatively charged MoS_2 nanosheets through electrostatic interaction, and then loaded indocyanine green (ICG) to prepare an efficient, low-power irradiation nanoplatform (Au/MoS_2-ICG) for synergistic cancer phototherapy (Fig. 16A).[83] In the Au/MoS_2 nanoplatform, the photothermal conversion efficiency of dual plasmonic PTT nanoagent (Au/MoS_2) reached as high as 68.8% under 808 nm laser radiation. More importantly, the high temperature caused by PTT promoted the release of ICG (85%) and the production of $^1O_2$, which was necessary for simultaneous PDT and PTT. Both *in vitro* and *in vivo* experiments showed the complete eradication of tumors, indicating that the synergistic therapeutic effect induced by Au/MoS_2-ICG was more significant than that induced by PDT or PTT alone. At the same time, the great biocompatibility of such composite has been verified as well.

However, ICG in the aforementioned nanoplatforms had poor stability and water solubility and accumulated well in tumors. Hence, Liu *et al.* used PDA and hyaluronic acid to modify ICG-loaded $MoSe_2$ nanoparticles and synthesized a highly stable nanosystem ($MoSe_2$@ICG-PDA-hyaluronic acid).[121] With the modification of PDA and hyaluronic acid, the products would significantly enhance the stability and accumulation of ICG in tumors, thereby producing a large amount of ROS to inhibit cancer cell growth. Meanwhile, under the irradiation of NIR light, $MoSe_2$ would generate abundant heat energy to kill cancer cells (Fig. 16B). In summary, $MoSe_2$@ICG-PDA-hyaluronic acid exhibited an excellent ability to inhibit tumor growth and metastasis through synergistic PDT/PTT.

In another recent study conducted by Qi *et al.*, MoS_2 nanosheets were modified with BSA (BSA-MoS_2) and loaded onto oxidized sodium alginate (OSA) and hydroxypropyl chitosan (HPCS) to synthesize an injectable and self-healing polysaccharide hydrogel (OSA-HPCS/BSA-MoS_2).[122] Owing to the reversible Schiff base bond formed between OSA and HPCS, the composite could be directly injected into the tumor site to avoid the loss of BSA-MoS_2 in the blood. Subsequently, under 808 nm laser irradiation, BSA-MoS_2 effectively killed tumor cells through the generation of ROS (Fig. 16C) along with photothermal conversion (Fig. 16D). Both *in vitro*/*vivo* investigations proved that BSA-MoS_2 could effectively eradicate cancer cells under NIR irradiation and was highly biocompatible.

Li *et al.* used MoS_2 as a carrier to load ICG and curcumin (Cur), and synthesized an ICG@Cur@MoS_2 nanoplatform applied for phototherapy.[123] During the study, Cur was proven to be efficient in inhibiting the activity of P-glycoprotein (P-gp), which is highly expressed in liver cells and will significantly decrease the activity of ICG. Therefore, the activity of ICG increased together with the effect of PDT. Through *in vitro*/vivo investigations, the ICG@Cur@MoS_2 nanoplatform further exhibited excellent photothermal effects, low toxicity, and efficient anti-tumor effects.

In addition to these materials above, metal ions doped into TMDs for phototherapy have also been explored. Zhou *et al.* successfully developed Eu^{3+}-doped MoS_2 (MoS_2:Eu^{3+}) nanoflowers *via* a hydrothermal method.[124] Under 808 nm laser radiation, the photothermal conversion efficiency of MoS_2:Eu^{3+} was significantly higher than that of pristine MoS_2 (Fig. 16E), which thus promoted the generation of ROS. Besides, *in vitro* experiments conducted on 4T1 cells showed exceptional anti-cancer effects of MoS_2:Eu^{3+} (Fig. 16F) as well as great biocompatibility and high photostability. Overall, with the synergistic effects of hyperthermia and generation of cytotoxic substances, the efficacy of cancer treatments based on TMDs under NIR irradiation can be dramatically enhanced.

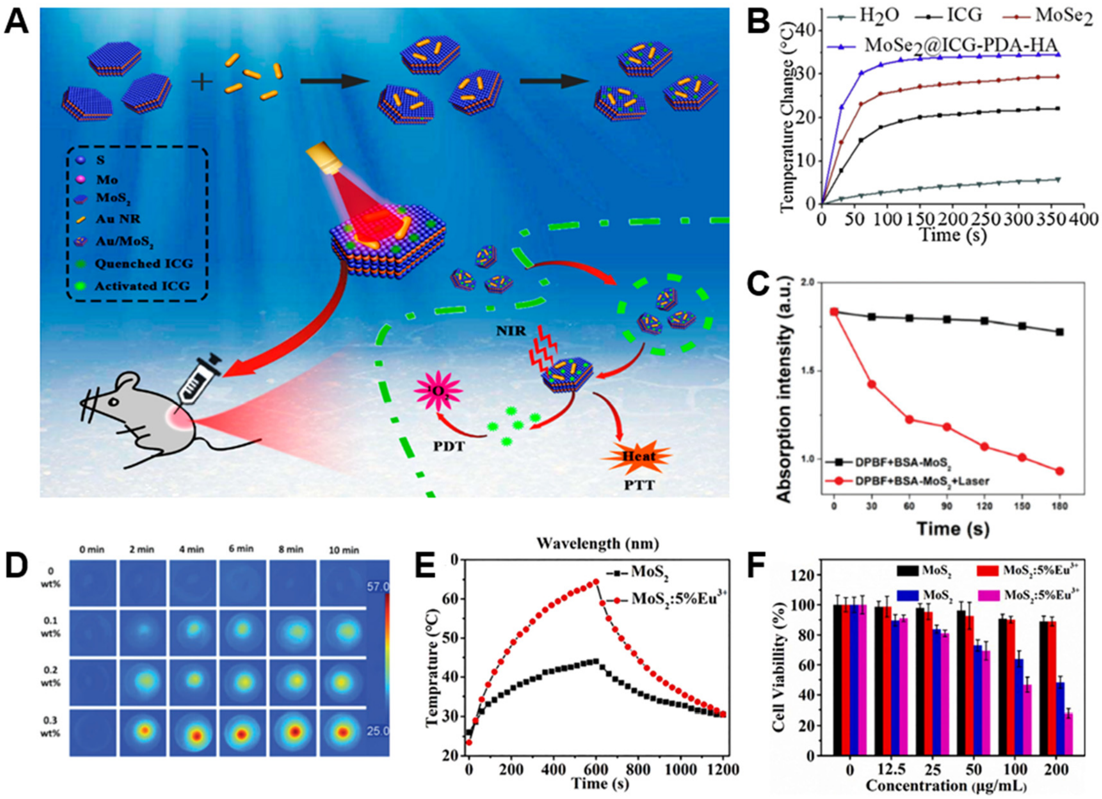

Fig. 16 TMD-based composites for phototherapy. (A) Schematic illustration of Au/MoS_2-ICG nanoplatform for tumor treatment.[83] Reproduced with permission from ref. 83. Copyright 2019 American Chemical Society. (B) Temperature change curves of various groups of different treatments under 808 nm laser.[121] Reproduced with permission from ref. 121. Copyright 2020 Elsevier. (C) Absorption intensity change of 1,3-diphenylisobenzofuran (DPBF) in various treatment groups after laser irradiation for a fixed time. (D) Infrared thermography of OSA-HPCS/BSA-MoS_2 with different BSA-MoS_2 concentrations under an NIR laser.[122] Reproduced with permission from ref. 122. Copyright 2022 Wiley-VCH. (E) Heating and cooling curves of MoS_2 and MoS_2:5%Eu^{3+} at different times. (F) Cell viability changes of mice in each group at different concentrations.[124] Reproduced with permission from ref. 124. Copyright 2021 Elsevier.

5.4. Other combination therapy

Apart from the synergistic PDT/PTT described above, there are also some other dual-modality (*e.g.*, chemotherapy/PTT) and tri-modality (*e.g.*, PTT/radiotherapy/checkpoint blockade immunotherapy) therapies for treating tumors or cancer cells. The related mechanism is schematically shown in Fig. 17A.[125]

Lei *et al.* successfully designed mesoporous silica nanoparticles (MSN) for DOX loading and blocked it with tumor-homing/-penetrating peptide tLyp-1 modified WS_2 quantum dots (WS_2-HP).[99] With the assistance of tLyP-1. DOX@MSN-WS_2-HP was delivered to the tumor site and released along with two other substances, DOX@MSN-NH_2 and WS_2-HP. DOX was responsible for the surface of tumor cells, while the penetrating WS_2-HP would kill deep cancer cells in the presence of the NIR laser. In brief, the DOX@MSN-WS_2-HP nanoplatform with synergistic effects of chemotherapy and PTT was a prospective candidate for anti-tumor therapy (Fig. 17B and C).

In another study, Lei *et al.* proposed a multifunctional therapeutic agent for synergistic sonodynamic therapy/CDT (SDT/CDT) by doping iron onto vanadium disulfide (VS_2) nanosheets with PEG modification (Fe-VS_2-PEG).[126] SDT always uses ultrasound and sonosensitizers to treat local tumors, whereas CDT depends on $^{\bullet}OH$ produced by the Fenton reaction, which can achieve tumor-specific treatment. During the experiments, the Fe within the composite was found to be capable of extending the electron–hole recombination time and reducing the bandgap to enhance the SDT effect. Additionally, Fe-VS_2-PEG could trigger the Fenton reaction under H_2O_2 conditions to produce $^{\bullet}OH$ (Fig. 17D) for CDT and consume glutathione (GSH), further enhancing the synergistic anti-cancer effect. In general, Fe-VS_2-PEG exhibited excellent cancer cell killing ability and low toxicity (Fig. 17E).

Beyond that, Yang *et al.* obtained WS_2-iron oxide/SiO_2@MnO_2-PEG (WS_2-IO/S@MO-PEG) nanoparticles by adsorbing iron oxide nanoparticles (IONP) onto the surface of WS_2 and coating them with SiO_2 together with MnO_2 for synergistic PTT/radiotherapy (PTT/RT).[127] The composite took advantage of the strong NIR absorption ability of WS_2 for PTT, and MnO_2 would accelerate the release of H_2O_2 to alleviate O_2 deficiency and enhance RT. As a result, in 4T1 tumor-bearing mouse models, such nanocomposites caused significant

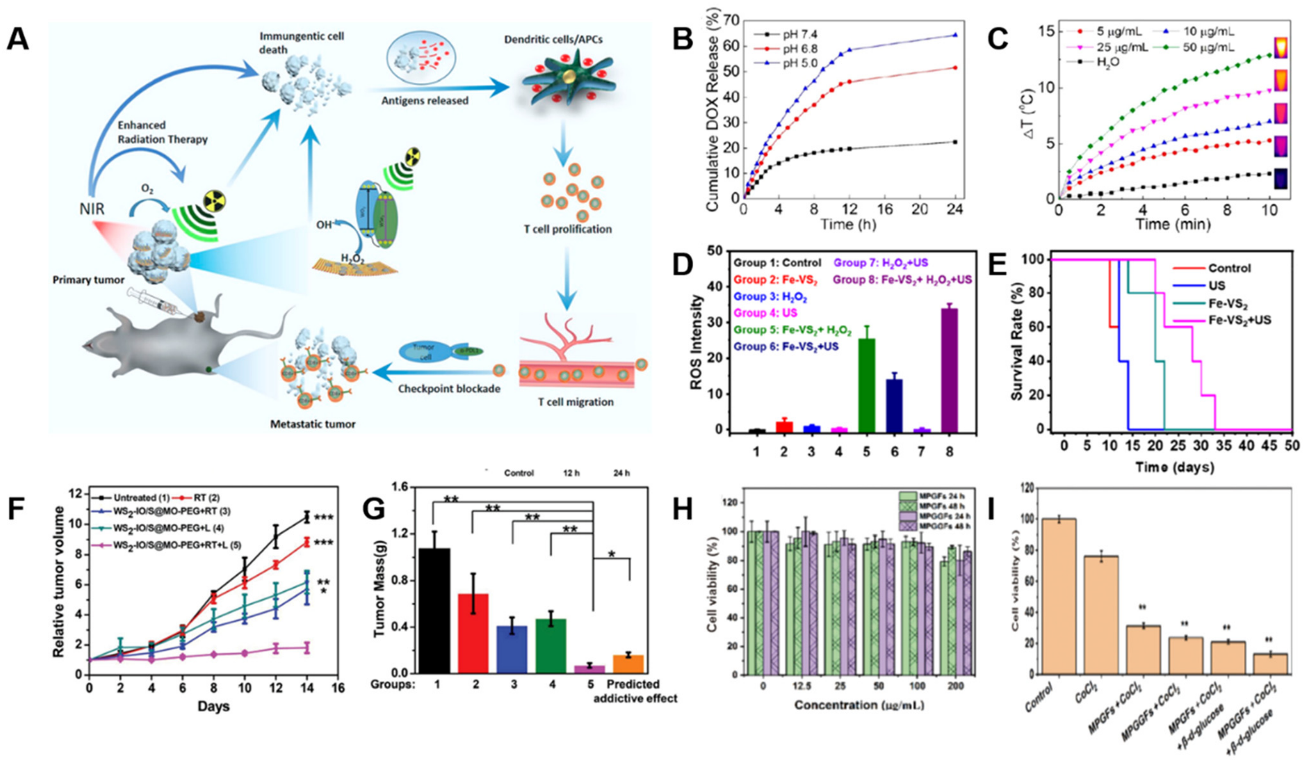

Fig. 17 TMD-based composites for combination therapy. (A) Schematic illustration of $WO_{2.9}$-WSe_2-PEG nanoparticles for combination therapy.[125] Reproduced with permission from ref. 125. Copyright 2020 American Chemical Society. (B) Cumulative DOX release curves from DOX@MSN-WS_2-HP under various pH conditions. (C) Temperature change of water and different concentrations of WS_2-HP under laser irradiation.[99] Reproduced with permission from ref. 99. Copyright 2017 American Chemical Society. (D) ROS levels in the cells after various treatments. (E) Survival rate of mice after various treatments of control, US only, Fe-VS_2, and Fe-VS_2 + US during 50 days of treatment.[126] Reproduced with permission from ref. 126. Copyright 2020 American Chemical Society. (F) Relative tumor growth and (G) average weight of mice in various treatment groups.[127] Reproduced with permission from ref. 127. Copyright 2018 Wiley-VCH. (H) Cell viability of L929 cells treated with MoS_2 nanoflowers modified with GOx (MPGFs) and MPGGFs for 24 hours or 48 hours, respectively. (I) Cell viability of 4T1 cells for the diverse treatment groups in control, $CoCl_2$, MPGFs + $CoCl_2$, MPGFs + $CoCl_2$ + β-D-glucose, MPGGFs + $CoCl_2$ + β-D-glucose.[128] Reproduced with permission from ref. 128. Copyright 2022 Tsinghua University Press.

necrosis and apoptosis of tumor cells (Fig. 17F,G) without obvious toxicity.

Except for the aforementioned dual-modality treatments, triple-modality therapies are also widely used against cancer. Dong *et al.* prepared a $WO_{2.9}$-WSe_2 heterostructure (WSP nanoparticles) by selenizing $WO_{2.9}$ nanoparticles through a hydrothermal method.[125] These WSP nanoparticles were applied for PTT owing to their strong NIR absorption ability, high photothermal conversion efficiency, high temperature, and increased oxygen levels resulting from PTT, thereby promoting RT. Subsequently, the combined treatment of PTT/RT was demonstrated to enhance the sensitivity of tumor immune antigens to checkpoint blockade immunotherapy (CBT), which was mainly reflected in the fact that anti-PD-L1 antibodies blocked the combination of programmed death ligand-1 (PD-L1) and programmed death receptor-1 (PD-1) to restore the recognition of the immune system and attack cancer cells (Fig. 17A). *In vitro* experimental results showed that WSP nanoparticles had the most significant therapeutic effect under X-ray and NIR laser irradiation, with a cancer cell survival rate of only 3.9%. *In vivo* experiments further confirmed the most significant tumor inhibition effect of WSP nanoparticles under X-ray and NIR, together with primary tumors regressing by more than 90% and distant tumors regressing by more than 80%.

Xie *et al.* modified MoS_2 nanoflowers with 2-deoxy-D-glucose (2-DG) and glucose oxidase (GOx) to synthesize multifunctional nanocatalysts (MPGGFs) for PTT/CDT/immunotherapy.[128] Upon delivery to the tumor microenvironment, MPGGFs released GOx to consume glucose and oxygen, producing large amounts of H_2O_2. Then, MPGGFs catalyzed exogenous and endogenous H_2O_2 to generate ROS, leading to cell necrosis. At the same time, MPGGFs also had a high photothermal conversion efficiency, which amplified the CDT effect to a certain extent. Subsequently, CDT/PTT combination therapy-induced tumor cell apoptosis and tumor antigen release, along with specific T cells for immunotherapy. Finally, they further demonstrated the good biocompatibility (Fig. 17H) and anti-tumor effects of the composite (Fig. 17I) using 4T1 cell-bearing mouse models. Generally, MPGGFs exhibited great potential for cancer treatments.

6. Conclusions and outlook

In this review, we briefly introduced TMD-based materials and summarized their categorizations according to their components and structures, as well as preparation strategies of TMD-based composites. The enhanced performance and stability achieved through material modifications have positioned TMD-based composites as focal points for cancer therapy research. These composites have demonstrated significant therapeutic effects and are increasingly being utilized in multimodal therapies to achieve synergistic anti-cancer outcomes. Importantly, TMD-based composites show excellent biocompatibility, as they have a minimal impact on normal cells while targeting tumor cells through endocytosis. Compared to individual TMDs, these composites offer superior stability and therapeutic efficiency.

However, several challenges persist. First, the large-scale synthesis of TMD-based composites remains difficult, requiring advancements in scalable production techniques. Second, the systemic toxicity of these materials is not yet fully understood, raising concerns regarding their safe excretion and metabolism *in vivo*. Third, phase engineering has shown potential for developing materials with novel properties.[9,129–132] However, its application to TMD-based composites for cancer therapy is still in its infancy, necessitating further investigation. Finally, more in-depth studies are needed to unravel the mechanisms by which these composites interact with biological systems, thereby enabling the design of more effective therapeutic strategies. Addressing these issues is essential for transitioning TMD-based composites from laboratory research to clinical application.

In conclusion, TMD-based composites represent an exciting frontier in biomedical research. Their versatility and effectiveness in cancer therapy highlight their potential to drive advancements in cancer treatment strategies. Moving forward, combining TMDs with other materials to create more efficient composites will be the key to broadening their applications in cancer and other biomedical fields.

Data availability

No primary research results, software or code have been included and no new data were generated or analysed as part of this review.

Conflicts of interest

There are no conflicts to declare.

Acknowledgements

This work was financially supported by the Key Grant for Special Professors in Jiangsu Province (RK119STP23002), the Natural Science Research Start-up Foundation of Recruiting Talents of Nanjing University of Posts and Telecommunications (NY223016), the Project of State Key Laboratory of Organic Electronics and Information Displays, Nanjing University of Posts and Telecommunication (ZS030ZR24004 and ZS030ZR23034), 2024 Nanjing Science and Technology Innovation Program (NJKCZYZZ2024-06), and the Belt and Road "Innovation Cooperation Project of Jiangsu" (BZ2022011).

References

1 R. E. Graff, T. B. Cavazos, K. K. Thai, L. Kachuri, S. R. Rashkin, J. D. Hoffman, S. E. Alexeeff, M. Blatchins, T. J. Meyers, L. Leong, C. G. Tai, N. C. Emami, D. A. Corley, L. H. Kushi, E. Ziv, S. K. Van den Eeden, E. Jorgenson, T. J. Hoffmann, L. A. Habel, J. S. Witte and L. C. Sakoda, *Nat. Commun.*, 2021, **12**, 970.

2 R. L. Siegel, T. B. Kratzer, A. N. Giaquinto, H. Sung and A. Jemal, *CA Cancer J. Clin.*, 2025, **75**, 10–45.

3 M. H. Larson, W. Pan, H. J. Kim, R. E. Mauntz, S. M. Stuart, M. Pimentel, Y. Zhou, P. Knudsgaard, V. Demas, A. M. Aravanis and A. Jamshidi, *Nat. Commun.*, 2021, **12**, 2357.

4 L. C. Baird, *Nature*, 2023, **622**, 702–703.

5 R. Cai, H. Xiang, D. Yang, K.-T. Lin, Y. Wu, R. Zhou, Z. Gu, L. Yan, Y. Zhao and W. Tan, *J. Am. Chem. Soc.*, 2021, **143**, 16113–16127.

6 S. Wu, X. Liu, J. Ren and X. Qu, *Small*, 2019, **15**, e1904870.

7 X. Meng, Z. Liu, Y. Cao, W. Dai, K. Zhang, H. Dong, X. Feng and X. Zhang, *Adv. Funct. Mater.*, 2017, **27**, 1605592.

8 H. Chen, T. Liu, Z. Su, L. Shang and G. Wei, *Nanoscale Horiz.*, 2018, **3**, 74–89.

9 W. Zhai, Z. Li, Y. Wang, L. Zhai, Y. Yao, S. Li, L. Wang, H. Yang, B. Chi, J. Liang, Z. Shi, Y. Ge, Z. Lai, Q. Yun, A. Zhang, Z. Wu, Q. He, B. Chen, Z. Huang and H. Zhang, *Chem. Rev.*, 2024, **124**, 4479–4539.

10 V. T. Vu, M. C. Nguyen, W. K. Kim, V. D. Do, V. K. Dat and W. J. Yu, *Small Struct.*, 2024, **5**, 2300401.

11 H. Jiang, X. Zhang, K. Chen, X. He, Y. Liu, H. Yu, L. Gao, M. Hong, Y. Wang, Z. Zhang and Y. Zhang, *Nat. Mater.*, 2025, **24**, 188–196.

12 Q. Liang, Q. Zhang, X. Zhao, M. Liu and A. T. S. Wee, *ACS Nano*, 2021, **15**, 2165–2181.

13 D. Nutting, G. A. Prando, M. Severijnen, I. D. Barcelos, S. Guo, P. C. M. Christianen, U. Zeitler, Y. G. Gobato and F. Withers, *Nanoscale*, 2021, **13**, 15853–15858.

14 G. Cheng, Z. Guo, N. Goli, F. Podjaski, K. Zheng, J. Jiang, S. Ramadan, G. Kerherve, S. Tagliaferri, M. Och, N. Klein, M. Cattelan, S. Agnoli, M.-M. Titirici and C. Mattevi, *Nano Lett.*, 2025, **25**, 1775–1782.

15 X. Su, Y. Han, Z. Liu, L. Fan and Y. Guo, *J. Electroanal. Chem.*, 2020, **859**, 113868.

16 J. Zhao, H. Wu, J. Zhao, Y. Yin, Z. Zhang, S. Wang and K. Lin, *J. Nanobiotechnol.*, 2021, **19**, 36.

17 Y. Wang, J. Zhao, Z. Chen, F. Zhang, Q. Wang, W. Guo, K. Wang, H. Lin and F. Qu, *Biomaterials*, 2019, **217**, 119282.

18 M. S. Dar, P. Rosaiah, J. Bhagyalakshmi, S. Ahirwar, A. Khan, R. Tamizhselvi, V. R. M. Reddy, A. Palaniappan and N. K. Sahu, *Coord. Chem. Rev.*, 2025, **523**, 216247.

19 A. Karagianni, E. Alexandratou, M. Terrones and K. V. Kordatos, *Carbon*, 2025, DOI: 10.1016/j.carbon.2025.119986.

20 H. Liu, Z. Deng, Z. Zhang, W. Lin, M. Zhang and H. Wang, *Matter*, 2024, **7**, 977–990.

21 L. Khalili, G. Dehghan, H. Hamishehkar, L. G. Voskressensky and A. Khataee, *Coord. Chem. Rev.*, 2025, **525**, 216316.

22 L. Li, I. Soyhan, E. Warszawik and P. van Rijn, *Adv. Sci.*, 2024, **11**, 2306035.

23 M. Chang, M. Wang, B. Liu, W. Zhong, D. Jana, Y. Wang, S. Dong, A. Antony, C. Li, Y. Liu, Z. Zhao, J. Lin, W. Jiang and Y. Zhao, *ACS Nano*, 2024, **18**, 8143–8156.

24 A. Bigham, I. Fasolino, S. Borsacchi, C. Valente, L. Calucci, G. Turacchio, M. Pannico, M. Serrano-Ruiz, L. Ambrosio and M. G. Raucci, *Bioact. Mater.*, 2024, **35**, 99–121.

25 Y. Cao, L. Tang, C. Fu, Y. Yin, H. Liu, J. Feng, J. Gao, W. Shu, Z. Li, Y. Zhu and W. Wang, *Nano Lett.*, 2024, **24**, 6767–6777.

26 J. Wang, W. Yu, H. Shen, Y. Sang, H. Zhang, B. Zheng, X. Peng, Y. Hu, X. Ma, Z. Yang and F. Yu, *Adv. Sci.*, 2025, DOI: 10.1002/advs.202414779.

27 Y. Chen, Y. Wu, B. Sun, S. Liu and H. Liu, *Small*, 2017, **13**, 1603446.

28 J. Liu, C. Zhao, W. R. Chen and B. Zhou, *Coord. Chem. Rev.*, 2022, **469**, 214654.

29 L. Cheng, X. Wang, F. Gong, T. Liu and Z. Liu, *Adv. Mater.*, 2020, **32**, 1902333.

30 A. Li, L. Xu, Y. Jia, M. Yuan, J. Zhang, H. Liu, S. Liu, Y. Zhu, X. Wei, W. Tu, Y. He, S. Ni, X. Jiang and X. Zhang, *Small*, 2024, **20**, 2310964.

31 Y. Zhao, S.-B. Wang, A.-Z. Chen and R. K. Kankala, *Coord. Chem. Rev.*, 2022, **472**, 214765.

32 J. Wang, L. Sui, J. Huang, L. Miao, Y. Nie, K. Wang, Z. Yang, Q. Huang, X. Gong, Y. Nan and K. Ai, *Bioact. Mater.*, 2021, **6**, 4209–4242.

33 L. Yang, J. Wang, S. Yang, Q. Lu, P. Li and N. Li, *Theranostics*, 2019, **9**, 3992–4005.

34 G. Li, F. Meng, T. Lu, L. Wei, X. Pan, Z. Nong, M. Wei, C. Liao and X. Li, *J. Pharm. Pharmacol.*, 2021, **73**, 1128–1135.

35 L. Wang, D. Xu, L. Jiang, J. Gao, Z. Tang, Y. Xu, X. Chen and H. Zhang, *Adv. Funct. Mater.*, 2021, **31**, 2004408.

36 M. H. Shin, E. Y. Park, S. Han, H. S. Jung, D. H. Keum, G. H. Lee, T. Kim, C. Kim, K. S. Kim, S. H. Yun and S. K. Hahn, *Adv. Healthcare Mater.*, 2019, **8**, e1801036.

37 Z. Chen, X. Wei, Y. Zheng, Z. Zhang, W. Gu, W. Liao, H. Zhang, X. Wang, J. Liu, H. Li and W. Xu, *J. Nanobiotechnol.*, 2023, **21**, 333.

38 B. Shariati, M. T. Goodarzi, A. Jalali, N. Salehi and M. Mozaffari, *New J. Chem.*, 2023, **47**, 20100–20108.

39 T. Liu, C. Wang, X. Gu, H. Gong, L. Cheng, X. Shi, L. Feng, B. Sun and Z. Liu, *Adv. Mater.*, 2014, **26**, 3433–3440.

40 C. Murugan, H. Lee and S. Park, *J. Mater. Chem. B*, 2023, **11**, 1044–1056.

41 L. Sun, H. Bai, H. Jiang, P. Zhang, J. Li, W. Qiao, D. Wang, G. Liu and X. Wang, *Colloids Surf., B*, 2022, **214**, 112462.

42 J. Cui, P. Li, J. Zhou, W.-Y. He, X. Huang, J. Yi, J. Fan, Z. Ji, X. Jing, F. Qu, Z. G. Cheng, C. Yang, L. Lu, K. Suenaga, J. Liu, K. T. Law, J. Lin, Z. Liu and G. Liu, *Nat. Commun.*, 2019, **10**, 2044.

43 M. Chhowalla, H. S. Shin, G. Eda, L.-J. Li, K. P. Loh and H. Zhang, *Nat. Chem.*, 2013, **5**, 263–275.

44 Y. Chen, Z. Lai, X. Zhang, Z. Fan, Q. He, C. Tan and H. Zhang, *Nat. Rev. Chem.*, 2020, **4**, 243–256.

45 X. Ding, F. Peng, J. Zhou, W. Gong, G. Slaven, K. P. Loh, C. T. Lim and D. T. Leong, *Nat. Commun.*, 2019, **10**, 41.

46 S. Manzeli, D. Ovchinnikov, D. Pasquier, O. V. Yazyev and A. Kis, *Nat. Rev. Mater.*, 2017, **2**, 17033.

47 R. Torres-Cavanillas, M. Morant-Giner, G. Escorcia-Ariza, J. Dugay, J. Canet-Ferrer, S. Tatay, S. Cardona-Serra, M. Giménez-Marqués, M. Galbiati, A. Forment-Aliaga and E. Coronado, *Nat. Chem.*, 2021, **13**, 1101–1109.

48 R. Wu, H. Zhang, H. Ma, B. Zhao, W. Li, Y. Chen, J. Liu, J. Liang, Q. Qin, W. Qi, L. Chen, J. Li, B. Li and X. Duan, *Chem. Rev.*, 2024, **124**, 10112–10191.

49 X. Song, R. Singha, G. Cheng, Y.-W. Yeh, F. Kamm, J. F. Khoury, B. L. Hoff, J. W. Stiles, F. Pielnhofer, P. E. Batson, N. Yao and L. M. Schoop, *Sci. Adv.*, 2023, **9**, eadd6167.

50 X. Zhang, Z. Lai, C. Tan and H. Zhang, *Angew. Chem., Int. Ed.*, 2016, **55**, 8816–8838.

51 S. Wang, J. Zhao, H. Yang, C. Wu, F. Hu, H. Chang, G. Li, D. Ma, D. Zou and M. Huang, *Acta Biomater.*, 2017, **58**, 442–454.

52 V. Yadav, S. Roy, P. Singh, Z. Khan and A. Jaiswal, *Small*, 2019, **15**, 1803706.

53 A. Chaturvedi, B. Chen, K. Zhang, Q. He, G.-H. Nam, L. You, Z. Lai, C. Tan, T. H. Tran, G. Liu, J. Zhou, Z. Liu, J. Wang, E. H. T. Teo and H. Zhang, *SmartMat*, 2020, **1**, e1011.

54 Q. Zhang, D. Geng and W. Hu, *SmartMat*, 2023, **4**, e1177.

55 S. Meng, Y. Zhang, H. Wang, L. Wang, T. Kong, H. Zhang and S. Meng, *Biomaterials*, 2021, **269**, 120471.

56 Q. Feng, N. Mao, J. Wu, H. Xu, C. Wang, J. Zhang and L. Xie, *ACS Nano*, 2015, **9**, 7450–7455.

57 Y. Pang, Y. Liu, M. Gao, L. Ouyang, J. Liu, H. Wang, M. Zhu and H. Pan, *Nat. Commun.*, 2014, **5**, 3519.

58 A. Koma and K. Yoshimura, *Surf. Sci.*, 1986, **174**, 556–560.

59 M. Alahmadi, W. S. Mohamed, A. Zhukov, M. Salaheldeen, W. H. Alsaedi, D. Alhashmialameer, K. Al-Ghamdi and A. M. Abu-Dief, *Inorg. Chem. Commun.*, 2023, **157**, 111336.

60 M. V. Santhosh, R. Geethu and K. S. Devaky, *J. Mater. Sci.: Mater. Electron*, 2023, **34**, 385.

61 H. Yan, J. Li, D. Liu, X. Jing, D. Wang and L. Meng, *CrystEngComm*, 2018, **20**, 2330.

62 W. Shi, S. Song and H. Zhang, *Chem. Soc. Rev.*, 2013, **42**, 5714–5743.

63 X. Lin, J. Wang, Z. Chu, D. Liu, T. Guo, L. Yang, Z. Huang, S. Mu and S. Li, *Chin. Chem. Lett.*, 2020, **31**, 1124–1128.

64 Y. Huang, Y.-H. Pan, R. Yang, L.-H. Bao, L. Meng, H.-L. Luo, Y.-Q. Cai, G.-D. Liu, W.-J. Zhao, Z. Zhou, L.-M. Wu, Z.-L. Zhu, M. Huang, L.-W. Liu, L. Liu, P. Cheng, K.-H. Wu, S.-B. Tian, C.-Z. Gu, Y.-G. Shi, Y.-F. Guo, Z. G. Cheng, J.-P. Hu, L. Zhao, G.-H. Yang, E. Sutter, P. Sutter, Y.-L. Wang, W. Ji, X.-J. Zhou and H.-J. Gao, *Nat. Commun.*, 2020, **11**, 2453.

65 S. Xu, Y. Zhong, C. Nie, Y. Pan, M. Adeli and R. Haag, *Macromol. Biosci.*, 2021, **21**, 2100233.

66 T. Liu, C. Wang, W. Cui, H. Gong, C. Liang, X. Shi, Z. Li, B. Sun and Z. Liu, *Nanoscale*, 2014, **6**, 11225.

67 Y. Long, X. Wu, Z. Li, J. Fan, X. Hu and B. Liu, *Biomater. Sci.*, 2020, **8**, 5088–5105.

68 H. Jiang, Y. Du, L. Chen, M. Qian, Y. Yang, T. Huo, X. Yan, T. Ye, B. Han, Y. Wang and R. Huang, *Int. J. Pharm.*, 2020, **586**, 119606.

69 D. Babai, I. Pinkas, D. Naveh and R. Tenne, *Nanoscale*, 2024, **16**, 9917–9934.

70 Z. Feng, X. Liu, L. Tan, Z. Cui, X. Yang, Z. Li, Y. Zheng, K. W. K. Yeung and S. Wu, *Small*, 2018, **14**, 1704347.

71 K. Kasinathan, B. Murugesan, N. Pandian, S. Mahalingam, B. Selvaraj and K. Marimuthu, *Int. J. Biol. Macromol.*, 2020, **149**, 1019–1033.

72 L. Ding, Y. Chang, P. Yang, W. Gao, M. Sun, Y. Bie, L. Yang, X. Ma and Y. Guo, *Mater. Sci. Eng. C*, 2020, **117**, 111371.

73 Y. Chen, Y. Xianyu and X. Jiang, *Acc. Chem. Res.*, 2017, **50**, 310–319.

74 M. Xie, N. Yang, J. Cheng, M. Yang, T. Deng, Y. Li and C. Feng, *Colloids Surf., B*, 2020, **187**, 110631.

75 H. Zheng, B. Ma, Y. Shi, Q. Dai, D. Li, E. Ren, J. Zhu, J. Liu, H. Chen, Z. Yin, C. Chu, X. Wang and G. Liu, *Chem. Eng. J.*, 2021, **406**, 126888.

76 B. Geng, H. Qin, W. Shen, P. Li, F. Fang, X. Li, D. Pan and L. Shen, *Chem. Eng. J.*, 2020, **383**, 123102.

77 B. Geng, H. Qin, F. Zheng, W. Shen, P. Li, K. Wu, X. Wang, X. Li, D. Pan and L. Shen, *Nanoscale*, 2019, **11**, 7220.

78 S. Nandi, S. K. Bhunia, L. Zeiri, M. Pour, I. Nachman, D. Raichman, J.-P. M. Lellouche and R. Jelinek, *Chem. – Eur. J.*, 2017, **23**, 963–969.

79 F. Gao, D. Wang, T. Zhang, A. Ghosal, Z. Guo, Y. Miao, G. Li, X. Liu, J. Lu, J. Yu, H. Fan and L. Zhao, *Chem. Eng. J.*, 2020, **395**, 125032.

80 Y. Li, R. Jia, H. Lin, X. Sun and F. Qu, *Adv. Funct. Mater.*, 2020, **31**, 2008420.

81 S. K. Maji, S. Yu, K. Chung, M. S. Ramasamy, J. W. Lim, J. Wang, H. Lee and D. H. Kim, *ACS Appl. Mater. Interfaces*, 2018, **10**, 42068–42076.

82 T. Liu, S. Shen, Y. Huang, X. Zhang, Z. Lai, T. H. Tran, Z. Liu and L. Cheng, *Nanoscale*, 2019, **11**, 22788–22795.

83 M. R. Younis, C. Wang, R. An, S. Wang, M. A. Younis, Z.-Q. Li, Y. Wang, A. Ihsan, D. Ye and X.-H. Xia, *ACS Nano*, 2019, **13**, 2544–2557.

84 S. Su, J. Li, Y. Yao, Q. Sun, Q. Zhao, F. Wang, Q. Li, X. Liu and L. Wang, *ACS Appl. Bio Mater.*, 2019, **2**, 292–298.

85 D. Han, Y. Yan, J. Wang, M. Zhao, X. Duan, L. Kong, H. Wu, W. Cheng, X. Min and S. Ding, *Sens. Actuators, B*, 2019, **288**, 586–593.

86 R.-Y. Meng, Y. Zhao, H.-Y. Xia, S.-B. Wang, A.-Z. Chen and R. K. Kankala, *ACS Mater. Lett.*, 2024, **6**, 1160–1177.

87 C. Wu, S. Wang, J. Zhao, Y. Liu, Y. Zheng, Y. Luo, C. Ye, M. Huang and H. Chen, *Adv. Funct. Mater.*, 2019, **29**, 1901722.

88 G. Pidamaimaiti, X. Huang, K. Pang, Z. Su and F. Wang, *New J. Chem.*, 2021, **45**, 10296–10302.

89 L. Chen, J. Xu, Y. Wang and R. Huang, *J. Mater. Sci. Technol.*, 2021, **63**, 91–96.

90 G. Zeng, M. Liu, X. Liu, Q. Huang, D. Xu, L. Mao, H. Huang, F. Deng, X. Zhang and Y. Wei, *Appl. Surf. Sci.*, 2016, **387**, 399–405.

91 S. Wang, W. Xi, Z. Wang, H. Zhao, L. Zhao, J. Fang, H. Wang and L. Sun, *J. Mater. Chem. B*, 2020, **8**, 5891.

92 H. Yi, X. Zhou, C. Zhou, Q. Yang and N. Jia, *Biomater. Sci.*, 2021, **9**, 148–156.

93 L. Chen, X. Zhou, W. Nie, W. Feng, Q. Zhang, W. Wang, Y. Zhang, Z. Chen, P. Huang and C. He, *ACS Appl. Mater. Interfaces*, 2017, **9**, 17786–17798.

94 C. H. Park, S. Lee, G. Pornnoppadol, Y. S. Nam, S.-H. Kim and B. J. Kim, *ACS Appl. Mater. Interfaces*, 2018, **10**, 9023–9031.

95 J.-T. Wang, W. Zhang, W.-B. Wang, Y.-J. Wu, L. Zhou and F. Cao, *Biochem. Biophys. Res. Commun.*, 2019, **511**, 587–591.

96 O. A. Moses, M. I. Khan, Q. Fang, L. Qin, Z. U. Rehman, Y. Zhang, C. D. Feng, Y. Ma, X. Tang, C. Wu, M. L. Adam, D. Huang, H. Liu and L. Song, *Nanotechnology*, 2019, **30**, 065102.

97 O. A. Moses, M. I. Khan, Q. Fang, L. Qin, Z. U. Rehman, Y. Zhang, C. D. Feng, Y. Ma, X. Tang, C. Wu, M. L. Adam, D. Huang, H. Liu and L. Song, *Nanotechnology*, 2019, **30**, 065102.

98 B. Mao, T. Bao, J. Yu, L. Zheng, J. Qin, W. Yin and M. Cao, *Nano Res.*, 2017, **10**, 2667–2682.

99 Q. Lei, S. B. Wang, J. J. Hu, Y. X. Lin, C. H. Zhu, L. Rong and X. Z. Zhang, *ACS Nano*, 2017, **11**, 7201–7214.

100 B. Liu, C. Li, G. Chen, B. Liu, X. Deng, Y. Wei, J. Xia, B. Xing, P. A. Ma and J. Lin, *Adv. Sci.*, 2017, **4**, 1600540.

101 Y. Wang, F. Zhang, Q. Wang, P. Yang, H. Lin and F. Qu, *Nanoscale*, 2018, **10**, 14534–14545.

102 Y. Huang, Y. Zhao, Y. Liu, R. Ye, L. Chen, G. Bai and S. Xu, *Chem. Eng. J.*, 2021, **411**, 128610.

103 T. Levin, Y. Lampel, G. Savyon, E. Levy, Y. Harel, Y. Elias, M. Sinvani, I. Nachman and J.-P. Lellouche, *Sci. Rep.*, 2021, **11**, 18883.

104 J. Pan, X. Zhu, X. Chen, Y. Zhao and J. Liu, *Biomater. Sci.*, 2018, **6**, 372–387.

105 H. Lin, Y. Chen and J. Shi, *Chem. Soc. Rev.*, 2018, **47**, 1938–1958.

106 F. Bray, J. Ferlay, I. Soerjomataram, R. L. Siegel, L. A. Torre and A. Jemal, *CA Cancer J. Clin.*, 2018, **68**, 394–424.

107 X. Mei, T. Hu, Y. Wang, X. Weng, R. Liang and M. Wei, *Wiley Interdiscip. Rev.: Nanomed. Nanobiotechnol.*, 2020, **12**, e1596.

108 T. Hu, Z. Gu, G. R. Williams, M. Strimaite, J. Zha, Z. Zhou, X. Zhang, C. Tan and R. Liang, *Chem. Soc. Rev.*, 2022, **51**, 6126–6176.

109 X. Yu, C. Xu, J. Sun, H. Xu, H. Huang, Z. Gan, A. George, S. Ouyang and F. Liu, *J. Nanobiotechnol.*, 2024, **22**, 515.

110 M. Kanelli, N. M. Bardhan, M. Sarmadi, B. Eshaghi, S. K. Alsaiari, W. T. Rothwell, A. Pardeshi, D. Varshney, D. C. De Fiesta, H. Mak, V. Spanoudaki, N. Henning, A. Kumar, J. Han, A. M. Belcher, R. Langer and A. Jaklenec, *ACS Nano*, 2024, **18**, 30433–30447.

111 K. Kalantar-zadeh, J. Z. Ou, T. Daeneke, M. S. Strano, M. Pumera and S. L. Gras, *Adv. Funct. Mater.*, 2015, **25**, 5086–5099.

112 B. L. Li, M. I. Setyawati, L. Chen, J. Xie, K. Ariga, C.-T. Lim, S. Garaj and D. T. Leong, *ACS Appl. Mater. Interfaces*, 2017, **9**, 15286–15296.

113 X. Dong, W. Yin, X. Zhang, S. Zhu, X. He, J. Yu, J. Xie, Z. Guo, L. Yan, X. Liu, Q. Wang, Z. Gu and Y. Zhao, *ACS Appl. Mater. Interfaces*, 2018, **10**, 4284.

114 W. Long, H. Ouyang, C. Zhou, W. Wan, S. Yu, K. Qian, M. Liu, X. Zhang, Y. Feng and Y. Wei, *J. Mol. Liq.*, 2020, **307**, 112962.

115 P. F. Hsiao, R. Anbazhagan, H. C. Tsai, K. Rajakumari, S. J. Lin, S. Y. Lin, K. Y. Lee, C. Y. Kao, R. S. Chen and J. Y. Lai, *Mater. Sci. Eng., C*, 2020, **107**, 110330.

116 S. Ariyasu, J. Mu, X. Zhang, Y. Huang, E. K. L. Yeow, H. Zhang and B. Xing, *Bioconjugate Chem.*, 2017, **28**, 1059–1067.

117 B. Pang, H. Yang, L. Wang, J. Chen, L. Jin and B. Shen, *Colloids Surf., A*, 2021, **608**, 125506.

118 P. Chithaiah, S. Ghosh, A. Idelevich, L. Rovinsky, T. Livneh and A. Zak, *ACS Nano*, 2020, **14**, 3004–3016.

119 C. Wu, J. Zhang, X. Tong, P. Yu, J.-Y. Xu, J. Wu, Z. M. Wang, J. Lou and Y.-L. Chueh, *Small*, 2019, **15**, 1900578.

120 K. Kasinathan, K. Marimuthu, B. Murugesan, M. Sathaiah, P. Subramanian, P. Sivakumar, U. Swaminathan and R. Subbiah, *Int. J. Biol. Macromol.*, 2021, **190**, 520–532.

121 Y. Liu, C. Wei, A. Lin, J. Pan, X. Chen, X. Zhu, Y. Gong, G. Yuan, L. Chen, J. Liu and Z. Luo, *Colloids Surf., B*, 2020, **189**, 110820.

122 Y. Qi, Y. Yuan, Z. Qian, X. Ma, W. Yuan and Y. Song, *Macromol. Biosci.*, 2022, **22**, 2200161.

123 S. Li, S. Yang, C. Liu, J. He, T. Li, C. Fu, X. Meng and H. Shao, *Int. J. Nanomed.*, 2021, **16**, 433–442.

124 S. Zhou, X. Jiao, Y. Jiang, Y. Zhao, P. Xue, Y. Liu and J. Liu, *Appl. Surf. Sci.*, 2021, **552**, 149498.

125 X. Dong, R. Cheng, S. Zhu, H. Liu, R. Zhou, C. Zhang, K. Chen, L. Mei, C. Wang, C. Su, X. Liu, Z. Gu and Y. Zhao, *ACS Nano*, 2020, **14**, 5400–5416.

126 H. Lei, X. Wang, S. Bai, F. Gong, N. Yang, Y. Gong, L. Hou, M. Cao, Z. Liu and L. Cheng, *ACS Appl. Mater. Interfaces*, 2020, **12**, 52370–52382.

127 G. Yang, R. Zhang, C. Liang, H. Zhao, X. Yi, S. Shen, K. Yang, L. Cheng and Z. Liu, *Small*, 2018, **14**, 1702664.

128 W. Xie, J. Lu, Z. Guo, X. Guo, Y. Chi, J. Ye, J. Zhang, W. Xu, L. Zhao and Y. Wei, *Nano Res.*, 2022, **15**, 2253.

129 Q. Yun, Y. Ge, Z. Shi, J. Liu, X. Wang, A. Zhang, B. Huang, Y. Yao, Q. Luo, L. Zhai, J. Ge, Y. Peng, C. Gong, M. Zhao, Y. Qin, C. Ma, G. Wang, Q. Wa, X. Zhou, Z. Li, S. Li, W. Zhai, H. Yang, Y. Ren, Y. Wang, L. Li, X. Ruan, Y. Wu, B. Chen, Q. Lu, Z. Lai, Q. He, X. Huang, Y. Chen and H. Zhang, *Chem. Rev.*, 2023, **123**, 13489–13692.

130 B. Chen, Q. Yun, Y. Ge, L. Li and H. Zhang, *Acc. Mater. Res.*, 2023, **4**, 359–372.

131 Z. Li, L. Zhai, Q. Zhang, W. Zhai, P. Li, B. Chen, C. Chen, Y. Yao, Y. Ge, H. Yang, P. Qiao, J. Kang, Z. Shi, A. Zhang, H. Wang, J. Liang, J. Liu, Z. Guan, L. Liao, V. A. Neacşu, C. Ma, Y. Chen, Y. Zhu, C.-S. Lee, L. Ma, Y. Du, L. Gu, J.-F. Li, Z.-Q. Tian, F. Ding and H. Zhang, *Nat. Mater.*, 2024, **23**, 1355–1362.

132 Z. Li, Y. Yue, J. Peng and Z. Luo, *Chin. Chem. Lett.*, 2023, **34**, 107119.